Impact of the South China Sea Summer Monsoon on the Indian Ocean Dipole in CMIP5 Models

YAZHOU ZHANG,[a] JIANPING LI,[a,b] FEI ZHENG,[c] MIAO YU,[d] JUAN FENG,[d] AND CHENG SUN[d]

[a] *Frontiers Science Center for Deep Ocean Multispheres and Earth System, Key Laboratory of Physical Oceanography, Institute for Advanced Ocean Studies, Ocean University of China, Qingdao, China*
[b] *Laboratory for Ocean Dynamics and Climate, Pilot Qingdao National Laboratory for Marine Science and Technology, Qingdao, China*
[c] *State Key Laboratory of Numerical Modeling for Atmospheric Sciences and Geophysical Fluid Dynamics, Institute of Atmospheric Physics, Chinese Academy of Sciences, Beijing, China*
[d] *College of Global Change and Earth System Science, Beijing Normal University, Beijing, China*

(Manuscript received 21 July 2020, in final form 4 November 2020)

ABSTRACT: The impact of the South China Sea summer monsoon (SCSSM) on the Indian Ocean dipole (IOD) has been systematically investigated in observations. This study focuses on the ability of climate models participating in phase 5 of the Coupled Model Intercomparison Project (CMIP5) to reproduce the observed relationship between the SCSSM and IOD and the relevant physical mechanisms. All 23 models reproduce significant correlations between the SCSSM and IOD during boreal summer [June–August (JJA)], whereas the influence of the SCSSM on the IOD varies considerably across the CMIP5 models. To explore the causes, all models are divided into two groups. Models that successfully simulated both the correlations between the SCSSM and JJA IOD and of the SCSSM and JJA IOD with precipitation over the western North Pacific and Maritime Continent are classified as Type I, and these produce stronger low-level wind anomalies over the tropical southeastern Indian Ocean. The stronger low-level wind anomalies enhance local sea surface temperature (SST) anomalies via positive wind–evaporation–SST (WES) and wind–thermocline–SST (Bjerknes) feedbacks. This corresponds to a strengthening of IOD events due to the increased zonal gradient of SST anomalies over the tropical Indian Ocean. In contrast, Type II models perform poorly in representing the relationship between the SCSSM and JJA IOD or relevant physical processes, corresponding to weaker WES and Bjerknes feedbacks, and produce weaker IOD events. These results demonstrate that the better the model simulation of the critical physical processes, the larger contribution of the SCSSM to the IOD.

KEYWORDS: Indian Ocean; Monsoons; Atmosphere-ocean interaction; Model evaluation/performance; Interannual variability

1. Introduction

The Indian Ocean dipole (IOD), characterized by colder (warmer) sea surface temperature (SST) anomalies over the tropical western Indian Ocean and warmer (colder) SST anomalies over the tropical southeastern Indian Ocean during the positive (negative) phases, shows a remarkable interannual variation (Saji et al. 1999; Webster et al. 1999). The IOD affects not only the climate of the countries surrounding the Indian Ocean rim, such as Kenya, India, Indonesia, and Australia, but also the western tropical Pacific Ocean, East Asia, South America, and even Antarctica through atmospheric teleconnection, causing extreme weather or climate events with severe socioeconomic repercussions (Ashok et al. 2003, 2004; Cai et al. 2009, 2011; Chen et al. 2020; Ding et al. 2010; Duan et al. 2020; Guan and Yamagata 2003; Li et al. 2011a,b; Nuncio and Yuan 2015; Saji and Yamagata 2003). Therefore, a comprehensive understanding of the driving factors, seasonal evolution, physical processes, and prediction of the IOD has great social and economic significance, with implications for prevention and mitigation of socioeconomic losses and sustainable development.

Previous studies have indicated that a positive (negative) IOD generally corresponds to El Niño (La Niña), suggesting that El Niño–Southern Oscillation (ENSO) is the dominant factor controlling the interannual variation of the IOD (Annamalai et al. 2003; Behera et al. 2006; Huang and Shukla 2007a; Krishnamurthy and Kirtman 2003; Schott et al. 2009; Stuecker et al. 2017; Xie et al. 2002; Yang et al. 2015; Zhang et al. 2015); however, not all IOD events coexist with the ENSO (Behera et al. 2006; Huang and Shukla 2007b; Saji et al. 1999; Webster et al. 1999; Yamagata et al. 2003; Zhang et al. 2018, 2019). This indicates that other external factors influence the evolution of the IOD. Based on long-term simulations excluding ENSO forcing, Huang and Shukla (2007b) concluded that fluctuations observed in the northwestern Pacific monsoon could be a significant control on the IOD during boreal summer [June–August (JJA)]. In a more recent study, Zhang et al. (2018, 2019) indicated that IOD growth may also be impacted by the significant interannual variability of the South China Sea summer monsoon (SCSSM) over the western North Pacific Ocean.

Comprehensive coupled general circulation models are often used to assess the large-scale processes of climate dynamics. A suite of state-of-the-art climate models are used in phase 5 of the Coupled Model Intercomparison Project (CMIP5), providing abundant ensemble data for scientific studies related

Corresponding author: Jianping Li, ljp@ouc.edu.cn

DOI: 10.1175/JCLI-D-20-0582.1

TABLE 1. Details of the CMIP5 models used in this study. Values in parentheses for the horizontal grid size denote the spectral truncation of the model (full names of models and institutes are available online at http://www.ametsoc.org/PubsAcronymList).

Model name	Run used	Modeling center/country	Horizontal grid (lat × lon)
ACCESS1.0	r1i1p1	CSIRO–BoM/Australia	144 × 192 (300 × 360)
ACCESS1.3	r1i1p1		
CCSM4	r1i1p1	NCAR/United States	192 × 288 (384 × 320)
CESM1(FASTCHEM)	r1i1p1	CESM/United States	192 × 288 (384 × 320)
CMCC-CM	r1i1p1	CMCC/Italy	240 × 480 (149 × 182)
CMCC-CMS	r1i1p1		96 × 192 (149 × 182)
CNRM-CM5	r1i1p1	CNRM–CERFACS/France	128 × 256 (292 × 362)
CSIRO Mk3.6.0	r1i1p1	CSIRO–QCCCE/Australia	96 × 192 (189 × 192)
FGOALS-g2	r1i1p1	LASG–IAP/China	108 × 128 (196 × 360)
GFDL-ESM2G	r1i1p1	NOAA GFDL/United States	90 × 144 (200 × 360)
GFDL-ESM2M	r1i1p1		
HadGEM2-AO	r1i1p1	Met Office/United Kingdom	144 × 192 (216 × 360)
HadGEM2-ES	r1i1p1		
INM-CM4.0	r1i1p1	INM/Russia	120 × 180 (340 × 360)
IPSL-CM5A-MR	r1i1p1	IPSL/France	143 × 144 (149 × 182)
MIROC5	r1i1p1	MIROC/Japan	128 × 256 (224 × 256)
MPI-ESM-LR	r1i1p1	MPI/Germany	96 × 192 (220 × 256)
MPI-ESM-MR	r1i1p1		96 × 192 (404 × 802)
MPI-ESM-P	r1i1p1		96 × 192 (220 × 256)
MRI-CGCM3	r1i1p1	MRI/Japan	160 × 320 (368 × 360)
MRI-ESM1	r1i1p1		
NorESM1-M	r1i1p1	Norwegian Climate Centre/Norway	96 × 144 (384 × 320)
NorESM1-ME	r1i1p1		

to the IOD (Taylor et al. 2012). For example, Liu et al. (2011, 2014) quantitatively examined the relative contributions of the dynamic and thermodynamic feedback processes during IOD events using output from CMIP3 and CMIP5 models. Guo et al. (2015) identified three types of IOD events based on observations and CMIP5 models. Cai et al. (2013, 2014, 2018) investigated the response of the frequency of IOD events—particularly extreme positive events—to greenhouse warming. Li et al. (2015, 2016) focused on the model biases related to the excessive IOD in CMIP5 model simulation and projection and examined the role of the precipitation bias over the tropical western Pacific in projecting the Indian summer monsoon rainfall (Li et al. 2017). Fan et al. (2017) investigated the coevolution of various types of El Niño and the IOD in observations and CMIP5 models. However, the aforementioned studies only focused on the IOD or IOD–ENSO connection; whether the CMIP5 models reproduce the relationship between the SCSSM and IOD is still unresolved. Here, we attempt to diagnose the impact of the SCSSM on the IOD and the relevant physical mechanisms using CMIP5 model simulations.

The remainder of this paper is organized as follows. Section 2 presents a brief review of the datasets and methods used in this study. Before testing the relationship between the SCSSM and IOD, the performance of CMIP5 models in simulating the climatology of the SCSSM and the IOD pattern is first evaluated in section 3. Section 4 systematically compares the impact of the SCSSM on the IOD and the relevant physical mechanisms in the observations and two types of CMIP5 models, with a focus on the ability of the models to reproduce the atmospheric bridges related to the SCSSM, that is, the precipitation dipole and SCSSM Hadley circulation. We further discuss the potential role of ENSO in the relationship between the SCSSM and the IOD in section 5. Section 6 provides a summary and discussion.

2. Datasets and methods

a. Datasets

The monthly mean atmospheric horizontal and vertical wind, net surface latent heat fluxes, and the total precipitation rate (prate) are taken from the National Centers for Environmental Prediction–National Center for Atmospheric Research (NCEP–NCAR) Reanalysis-I (NCEP1), with a 2.5° × 2.5° horizontal grid (Kalnay et al. 1996). The improved Extended Reconstructed SST version 5 (ERSST v5) dataset on a 2° × 2° grid is used in this study (Huang et al. 2017). Sea surface height (SSH) is used to represent the thermocline variability (Yu 2003) and is obtained from the Simple Ocean Data Assimilation (SODA, version 2.2.4) reanalysis dataset on a 0.5° × 0.5° grid (Carton and Giese 2008). The study period 1948–2005 is chosen for the above datasets. To demonstrate the robustness of the results, precipitation from the Climate Prediction Center Merged Analysis of Precipitation (CMAP; Xie and Arkin 1997), wind from the NCEP–NCAR Reanalysis-II (NCEP2; Kanamitsu et al. 2002), and SST from the Met Office Hadley Centre SST (HadISST; Rayner et al. 2003) during 1979–2005 are also used in this study.

We used 23 CMIP5 models from the World Climate Research Program (WCRP) in this study for the period 1948–2005 (Table 1), while not all models include several realizations. Thus, the first realization (r1i1p1) of historical simulation outputs from 23 CMIP5 models is adopted in this study. Some models including several realizations (e.g., CNRM-CM5,

FGOALS-g2, and MPI-ESM-LR) are also examined, which is similar to the results of the first realization. Atmospheric and oceanic variables are downloaded from the CMIP5 multimodel data archive (https://esgf-node.llnl.gov/search/cmip5/), including 925-hPa wind, precipitation, vertical wind, SST, and SSH. To validate the CMIP5 historical simulations with respect to the observations, the atmospheric and oceanic variables in each model are linearly interpolated to 2.5° × 2.5° and 2° × 2° horizontal resolutions, respectively, when performing multimodel ensemble mean. To exclude the influence of global warming, the linear trend has been removed. In addition, the anomalies are calculated by subtracting the long-term (1979–2005) mean climatology from all datasets in this study.

The seasonal variation of winds is used by Li and Zeng (2002, 2003) to define the dynamical normalized seasonality monsoon index, which captures well the multiple variabilities of the global monsoon. This index is calculated as follows:

$$\delta = \frac{\|\overline{\mathbf{V}}_1 - \mathbf{V}_{m,n}\|}{\|\overline{\mathbf{V}}\|} - 2,$$

where $\overline{\mathbf{V}}_1$ and $\overline{\mathbf{V}}$ represent the climatological mean wind vectors in January and the mean of the January and July climatological wind vectors, respectively, and $\mathbf{V}_{m,n}$ denotes the monthly wind vectors in the mth month of the nth year. The SCSSM index (SCSSMI) is defined as an area average of δ over the SCSSM domain (100°–125°E, 0°–25°N) in the 925-hPa wind field during JJA. Wang et al. (2001) also defined the SCSSMI (also as western North Pacific monsoon index) based on the 850-hPa zonal wind anomalies between a southern region (100°–130°E, 5°–15°N) and a northern region (110°–140°E, 20°–30°N). The correlation coefficient between these two indices is 0.81 (beyond 99% confidence level, not shown), indicating the high consistence of these two indices to quantify the SCSSM variability. Compared the SCSSMI only based on the zonal wind in Wang et al. (2001), the SCSSMI defined by Li and Zeng (2002, 2003) takes both the zonal and meridional winds into consideration, showing more meridional circulation features related to SCSSM variability. Thus, the SCSSMI in Li and Zeng (2002, 2003) is adopted in this study.

The dipole mode index (DMI; Saji et al. 1999) can be used to measure IOD strength and is defined as the difference between area-averaged SST anomalies over the southeastern (90°–110°E, 10°S–0°) and western (50°–70°E, 10°S–10°N) tropical Indian Ocean; these SST anomalies are the IOD-E index (EDMI) and IOD-W index (WDMI), respectively. The Niño-3.4 index is used for monitoring ESNO variability, and is defined as the area average of SST anomalies over 170°E–120°W, 5°N–5°S.

b. Methods

According to previous studies (Fan et al. 2017; Guo et al. 2015; Saji et al. 1999; Schott et al. 2009; Yamagata et al. 2003), the IOD pattern can generally be identified as the second leading empirical orthogonal function (EOF) mode of the monthly SST anomalies over the tropical Indian Ocean (40°–120°E, 20°S–20°N). We employ a Taylor diagram (Taylor 2001) to provide a concise statistical summary of the match between observations and simulations; the modeled accuracy can be visually evaluated by individual points in the graph. Specifically, through comparison with the observations in terms of the correlations and ratio of standard deviations, we can clearly assess how well the models reproduce the observed pattern and magnitude. Correlation and regression analyses are also used to explore the relationship between the SCSSM and the IOD, and partial correlation is used to examine the potential role of ENSO in the SCSSM–IOD relationship.

The correlation coefficients between the SCSSM and the IOD are calculated for the observations and each of the CMIP5 models, and their significance is tested by a two-tailed Student's t test using the effective number of degrees of freedom (N_{eff}). For the variables X and Y, the significance between them can be approximated as follows (e.g., Bretherton et al. 1999; Li et al. 2013):

$$\frac{1}{N_{\text{eff}}} \approx \frac{1}{N} + \frac{2}{N}\sum_{i=1}^{N}\frac{N-i}{N}\rho_{XX}(i)\rho_{YY}(i),$$

where N is the total sample of time series, $\rho_{XX}(i)$ and $\rho_{YY}(i)$ denote the autocorrelations of the two time series X and Y at time lag i, respectively.

3. Relationship between the SCSSM and the IOD

a. Simulation of the SCSSM

The SCSSM is closely associated with wind and precipitation over both the western North Pacific Ocean and the Maritime Continent (Li and Zeng 2003; Wang et al. 2009; Zhang et al. 2018, 2019), showing remarkable regional large-scale circulation features. Hence, the ability of the CMIP5 models to reproduce the climatological mean 925-hPa wind and precipitation are first examined over the SCSSM-related domain (90°–160°E, 20°S–30°N) in JJA for the period 1976–2005. Taking NCEP1 as the reference, we employ a Taylor diagram (Taylor 2001) to quantitatively compare the performance of the model with respect to JJA 925-hPa wind and precipitation (Figs. 1a,b). For the climatological mean 925-hPa wind, the spatial correlation coefficients of the zonal wind between the simulations and observations exceed 0.85 for all historical model simulations, much larger than those for meridional wind (Fig. 1a). Likewise, all models also represent the spatial pattern of the precipitation climatology reasonably well, with spatial correlation coefficients exceeding 0.6 (Fig. 1b). In addition, the CMIP5 models (Fig. 2) capture reasonably well the centers of maximum precipitation, such as the western North Pacific, the South China Sea, and the northeast Bay of Bengal, similar to previous studies (Song and Zhou 2014a,b). These results indicate that the ability of the models to simulate these large-scale elements associated with the SCSSM is generally reasonable.

The simulated amplitudes of the 925-hPa wind and precipitation associated with the SCSSM are, however, significantly different from the observations. Most models overestimate the observed climatology of the 925-hPa wind and precipitation, with the ratio of the standard deviation of the modeled values to the observations being greater than 1.0, although some models generate underestimates (Figs. 1a,b). The modeled magnitude of the zonal wind tends to fit the observations a little

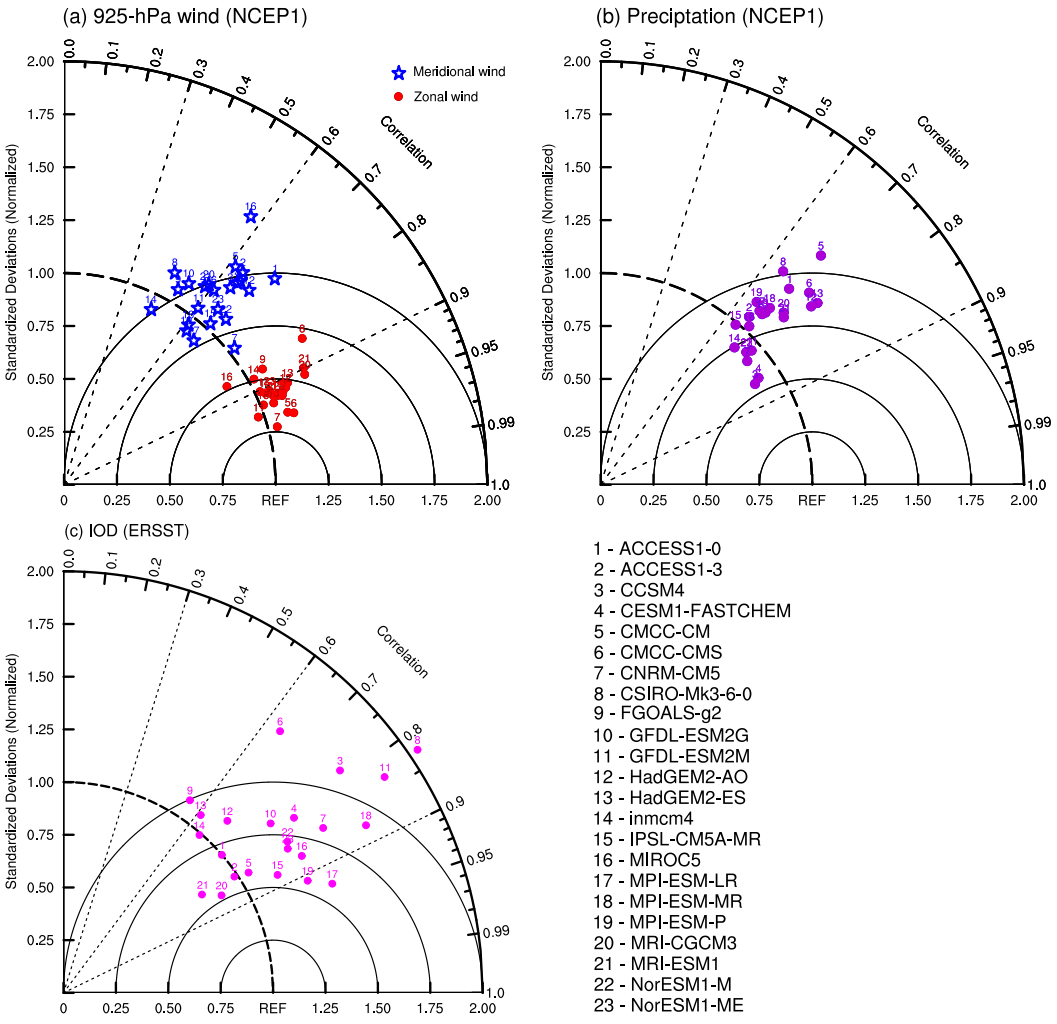

FIG. 1. Taylor diagrams of the climatological mean (a) 925-hPa zonal (red dots) and meridional (blue stars) wind and (b) precipitation (violet dots) over the SCSSM-related region (90°–160°E, 20°S–30°N) during boreal summer (JJA) for the period 1976–2005. (c) As in (a), but for the EOF2 pattern of SST anomalies over the tropical Indian Ocean (40°–120°E, 20°S–20°N) during 1948–2005 based on ERSST and CMIP5 models expect for EOF1 in CSIRO Mk3.6.0. The numbers represent the 23 models in CMIP5. The correlation coefficients and the ratio of the standard deviation between models and observations are shown by the cosine of the azimuth angle and the radial distance, respectively. REF (based on NCEP1) on the horizontal axis indicates the reference point.

better than the meridional wind and precipitation, with a smaller standard deviation (Figs. 1a,b).

b. *Simulation of the IOD*

As suggested by previous studies (Fan et al. 2017; Guo et al. 2015; Saji et al. 1999; Schott et al. 2009; Yamagata et al. 2003), the IOD can be represented by EOF2 of the SST anomalies over the tropical Indian Ocean, which is characterized by a zonal out-of-phase structure (Fig. 3). Notably, EOF1 of SST anomalies in CSIRO Mk3.6.0 is used to following analyses because EOF1 in CSIRO Mk3.6.0 displays the prominent IOD pattern (Fig. 3i). Spatial correlation coefficients between the models and observations exceed 0.5 for all models (Fig. 1c). This indicates that the models can reasonably simulate the IOD pattern, which is defined as the zonal alternations in SST over the tropical Indian Ocean (Fig. 3). Similar results are also obtained using the HadISST dataset, although with relatively lower spatial correlation coefficients (not shown). There are noticeable biases between the observed and modeled amplitudes of the IOD, similar to those for the SCSSM. The ratio of the standard deviation of the modeled to observed IOD patterns is less than 1.0 in the MRI-CGCM3 and MRI-ESM1. This indicates that these two models relatively underestimate the amplitude of the IOD pattern. In contrast, most of the CMIP5 models generally overestimate the amplitude of the IOD pattern.

Overall, the CMIP5 models agree well with the reanalysis data in simulating the spatial patterns of the IOD and the 925-hPa

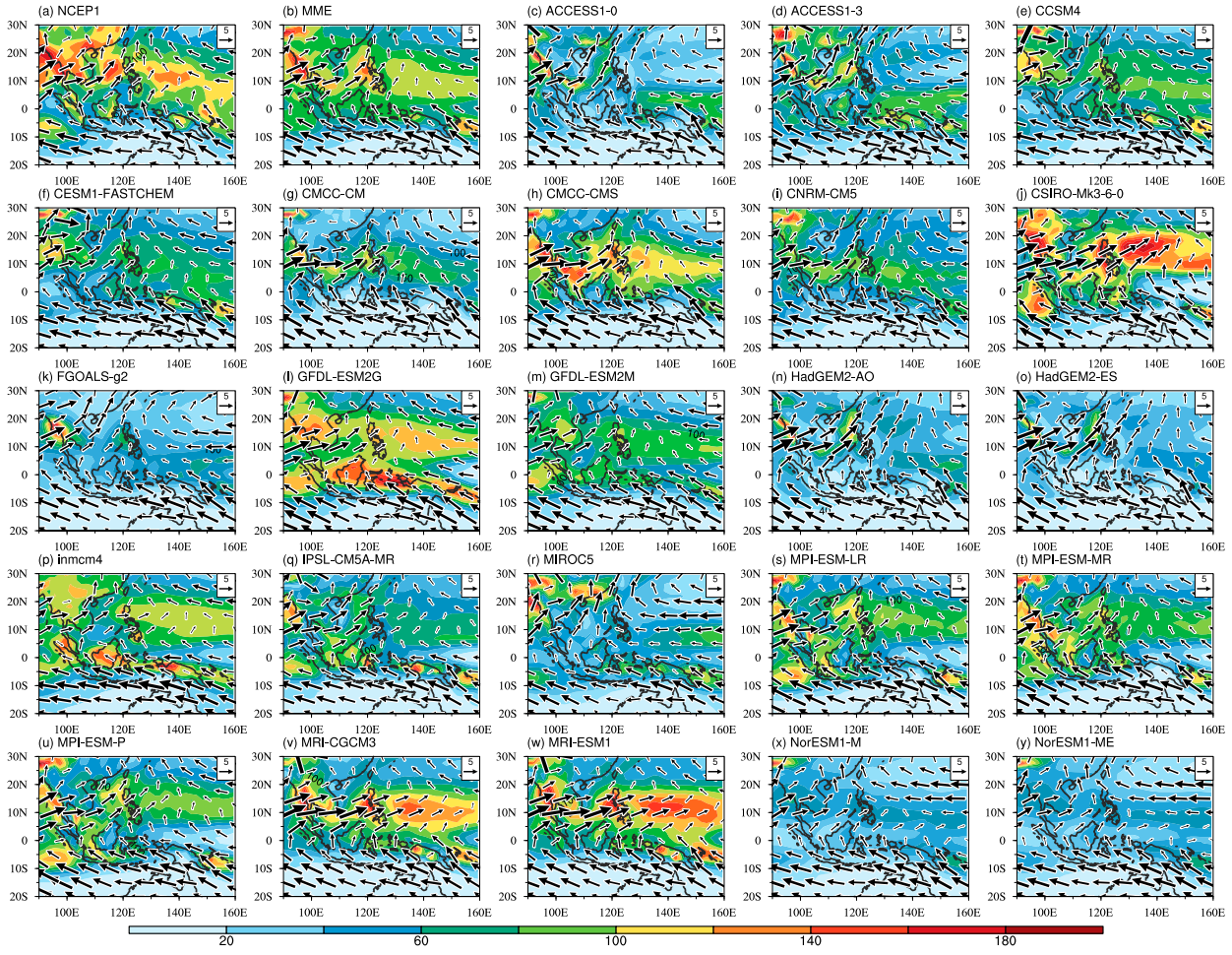

FIG. 2. Climatological mean JJA precipitation rate (shading; 10^5 kg m^{-2} s^{-1}) and 925-hPa wind (vectors; m s^{-1}) anomalies during 1976–2005 from (a) the observations (NCEP1), (b) MME, and (c)–(y) the individual 23 CMIP5 models.

wind and precipitation climatology, although there is still disparity in intensity. This indicates that all models have some skill in simulating the essential circulation features related to the SCSSM and the spatial patterns of the IOD. Moreover, the relatively reasonable simulations of the spatial structures of the SCSSM features and IOD provide the basic guarantee for assessing the performance of the CMIP5 models in simulating the relationship between the SCSSM and the IOD.

c. *Correlation between the SCSSM and IOD in CMIP5 models*

Figure 4 shows the correlation coefficients between the SCSSM and the IOD during JJA and boreal fall [September–November (SON)] for the observations and model simulations. The SCSSM is significantly correlated with the JJA IOD in the observations with a coefficient of 0.52 (Fig. 4a). Although the correlation coefficients between the SCSSM and JJA IOD vary with CMIP5 model, they are all significant, exceeding the 99% confidence level (Fig. 4a). As the SCSSM decays in SON, the SCSSM still has a maximum correlation coefficient with SON IOD with a value 0.59 (Fig. 4b; Zhang et al. 2018). Similar to JJA, the significant correlation coefficients between the SCSSM and SON IOD are also found in the observations and in each CMIP5 model (Fig. 4b). These results suggest that the significant correlations of the SCSSM with JJA and SON IOD are successfully reproduced in all CMIP5 models. This leads us to ask whether the mechanisms responsible for the influence of the SCSSM on the IOD are also reasonably simulated.

4. Possible physical mechanisms

Zhang et al. (2018, 2019) have indicated that the precipitation dipole and Hadley circulation associated with the SCSSM over the western North Pacific and the Maritime Continent serve as the "atmospheric bridges" between the SCSSM and the IOD. To further verify the aforementioned results, Fig. 5 displays the composite anomalies of the precipitation and 925-hPa wind based on the strong and weak SCSSM years in observations. Here, a strong (weak) SCSSM year is selected as the SCSSMI is greater (smaller) than 1 (−1) standard deviation. In a strong SCSSM year, the enhanced southeasterly wind anomalies bring more moisture from the north Indian Ocean to

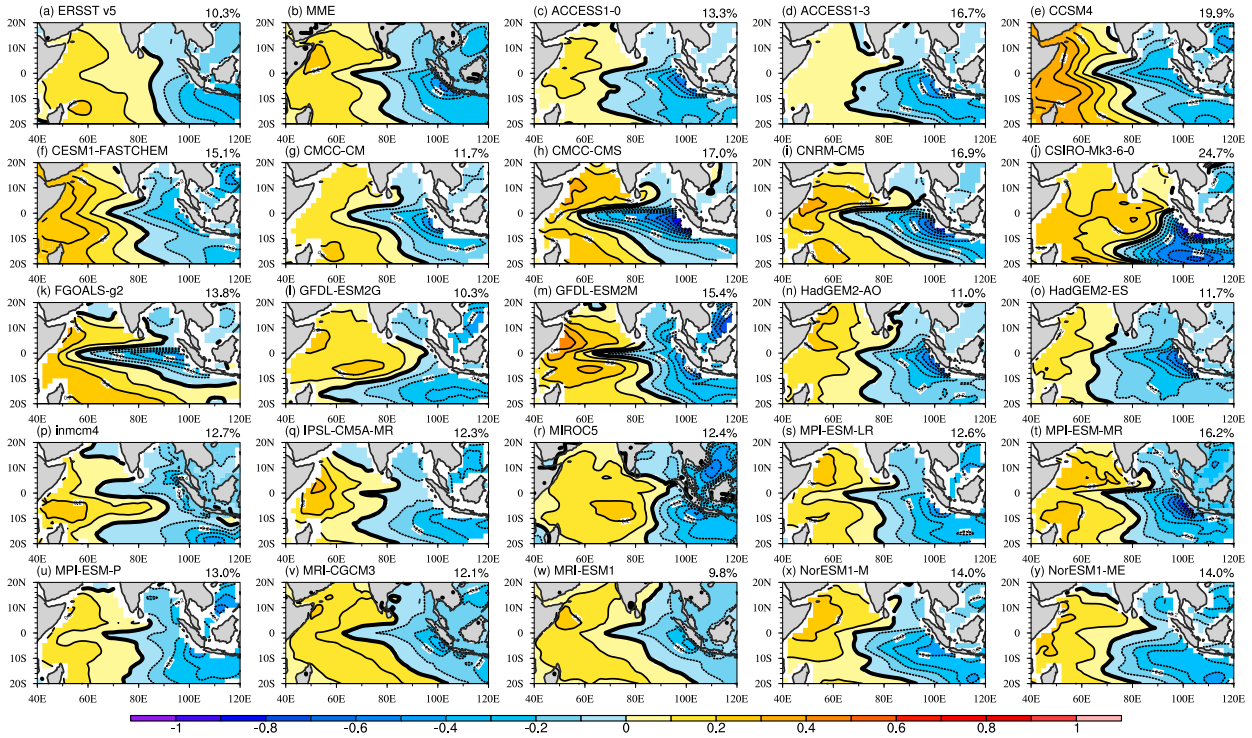

FIG. 3. Spatial pattern of the IOD as the second leading EOF mode of the tropical Indian Ocean (40°–120°E, 20°S–20°N) SST anomalies calculated from (a) observations (ERSST v5), (b) MME, and (c)–(y) the individual 23 CMIP5 models expect for first EOF mode in CSIRO Mk3.6.0. Values at the top right of each panel are the explained variance.

the western North Pacific (Fig. 5a), leading to surplus precipitation and further inducing the anomalous ascending motion over the western North Pacific (Fig. 5b). Consequently, the anomalous descending motion of the SCSSM Hadley circulation [the concept referred to in Zhang et al. (2018)] develops over the Maritime Continent, contributing to deficit precipitation over there (Fig. 5). With the enhancement of the precipitation dipole over the western North Pacific and Maritime Continent, the lower-level southerly wind anomalies prevail from the Maritime Continent to the western North Pacific. The southeasterly wind anomalies induced by the Coriolis force are strengthened over the tropical southeastern Indian Ocean (Fig. 5a; Zhang et al. 2018). On the one hand, overlaid on the climatological southeasterly wind in JJA, the enhanced southeasterly wind anomalies increase the excessive surface evaporation and latent heat flux loss from the ocean, leading to the intensification of the local cold SST anomalies. On the other hand, the increased southeasterly wind anomalies also tend to shallow local thermocline anomalies, bringing the deep cold water to the surface, and further cooling the local SST anomalies. Thus, the cold SST anomalies over the tropical southeastern Indian Ocean are strengthened under framework of positive WES and Bjerknes feedbacks. As the zonal SST anomaly gradient increases over the tropical Indian Ocean, a positive IOD event strengthens, and vice versa. Although the SCSSM withdraws in SON, the mature phase of the IOD may develop under the positive Bjerknes feedback. In next section, the physical mechanisms responsible for the influence of the SCSSM on the IOD are examined in CMIP5 models.

a. Atmospheric bridges associated with the SCSSM

Figure 6 shows the correlations of the SCSSMI with the 925-hPa wind and the precipitation for observations, multimodel ensemble (MME) mean, and each CMIP5 model during JJA. When the SCSSM is strong, the observed precipitation increases over the western North Pacific, and decreases over the Maritime Continent, producing a remarkable dipole pattern (Fig. 6a). Clear southeasterly wind anomalies are also observed over the tropical southeastern Indian Ocean. In addition, the circulation anomalies related to SCSSM show the evident longitudinal extent over the western North Pacific, which may be closed to the mean flow there. A climatological confluence zone covers the whole South China Sea (Fig. 2), aiding the zonally elongated perturbation via extracting kinetic energy from the mean flow (Hu et al. 2019). The MME mean can capture reasonably well this significant precipitation dipole pattern and the southeasterly wind anomalies over the tropical southeastern Indian Ocean (Fig. 6b).

However, there are some biases in the simulated amplitude and locations of the observed precipitation. The observed precipitation intensity over the western North Pacific is much stronger than that over the Maritime Continent, whereas the situation is reversed in the MME mean (Figs. 6a,b). This

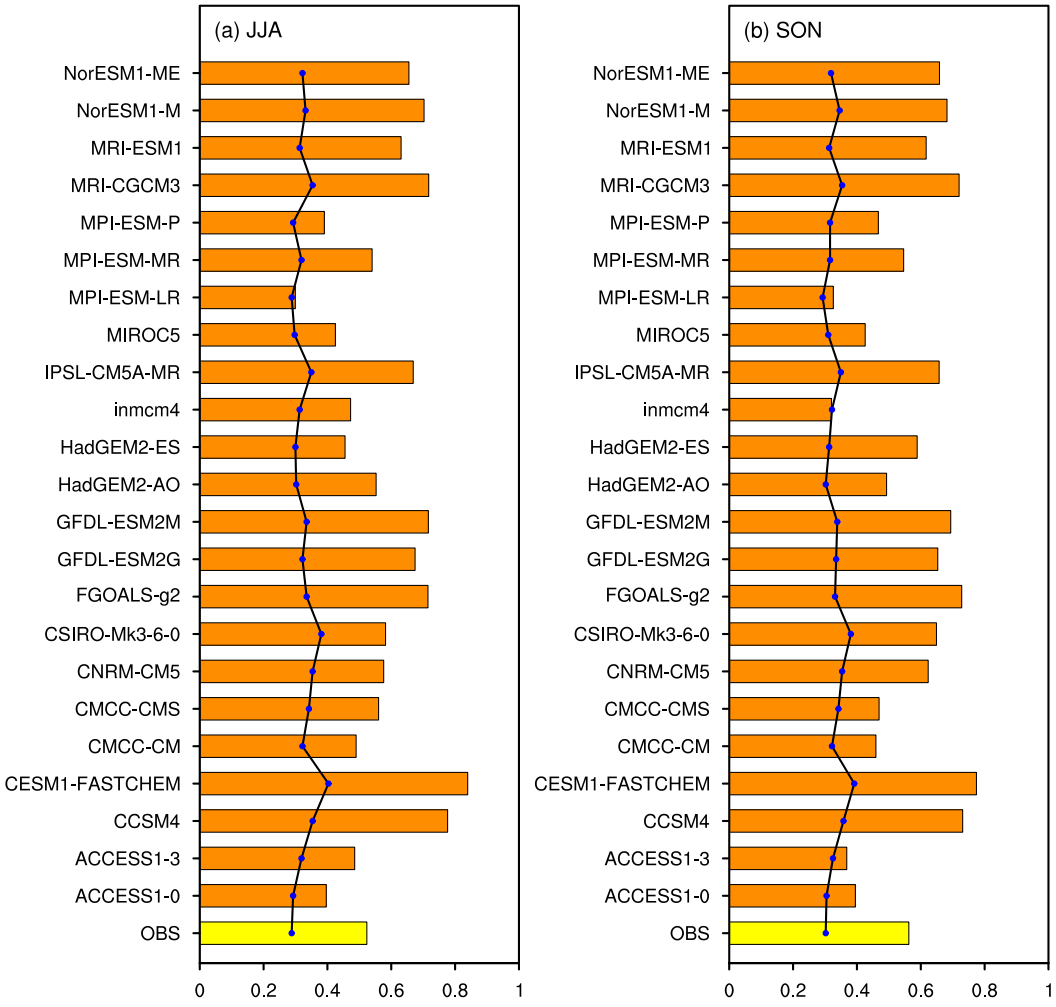

FIG. 4. Correlations of the SCSSMI with (a) JJA and (b) SON DMI for the period 1948–2005 for observations (yellow bar) and each model (orange bars); significance is tested by a two-tailed Student's t test using the effective number of degrees of freedom (black line with blue dots indicates the 99% confidence level).

indicates that the precipitation over the western North Pacific (Maritime Continent) is evidently underestimated (overestimated) in the MME mean (Fig. 6b). In addition, the simulated precipitation belt over the western North Pacific in the MME mean tends to occur farther south than observed (southward bias), whereas there is a relatively weak northward bias (farther north than observed) over the Maritime Continent (Fig. 6b). Similar results are seen for the observed and simulated SCSSM Hadley circulation (Fig. 7a). A significant SCSSM Hadley circulation is clearly seen over the western North Pacific and the Maritime Continent in the MME mean, accompanied by some biases in simulating its amplitude and location (Fig. 7b). The precipitation dipole pattern related to the SCSSM can essentially be simulated by the MME mean, but this relationship varies across the CMIP5 models (Fig. 6). Some models (e.g., CRISO-Mk3.6.0 and FGOALS-g2) can capture reasonably the prominent precipitation dipole pattern over the western North Pacific and the Maritime Continent (Figs. 6j,k), whereas other models, such as ACCESS1.0 and ACCESS1.3 (Figs. 6c,d), only successfully simulate the precipitation anomalies over the Maritime Continent. Similar results can also be found for the simulated SCSSM Hadley circulation (Fig. 7).

To describe objectively the relationship between the SCSSM and the precipitation dipole, the correlations between the SCSSM and JJA precipitation over the western North Pacific (115°–150°E, 5°–20°N) and Maritime Continent (100°–140°E, 15°S–0°) in observations and each model are shown in Fig. 8a. Compared to the significant correlations of the SCSSM with precipitation over both the western North Pacific and Maritime Continent in observation, the contrasting simulations exist in 23 models (Fig. 8a). Although the SCSSM is significantly correlated with precipitation over the Maritime Continent in all models, only 15 out of the 23 models [i.e., CCSM4, CESM1(FASTCHEM), CNRM-CM5, CSIRO Mk3.6.0, FGOALS-g2, GFDL-ESM2G, GFDL-ESM2M, HadGEM2-AO,

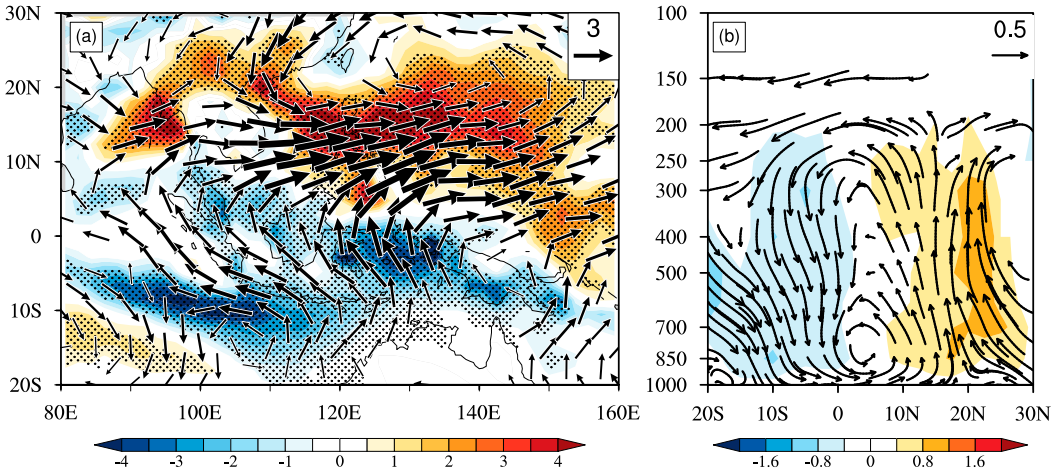

FIG. 5. (a) Composite difference in the precipitation (shading; 10^{-4} kg m^{-2} s^{-1}) and 925-hPa wind (vectors; m s^{-1}) anomalies during JJA between the strong and weak SCSSM years. (b) As in (a), but for the vertical pressure velocity anomalies (shading; -10^{-2} Pa s^{-1}) and the meridional–vertical circulation anomalies averaged between 90° and 150°E (vectors; m s^{-1}). Black stipples and vectors in (a) and (b) indicate that the composite anomalies are statistically significant at the 90% confidence level.

INM-CM4.0, IPSL-CM5A-MR, MPI-ESM-MR, MPI-ESM-P, MRI-CGCM3, NorESM1-M, and NorESM1-ME] successfully replicate the significant correlation between the SCSSM and the western North Pacific precipitation (Fig. 8a). The remaining eight models (i.e., ACCESS1.0, ACCESS1.3, CMCC-CM, CMCC-CMS, HadGEM2-ES, MIROC5, MPI-ESM-LR, and MRI-ESM1) cannot reproduce the relationship between the SCSSM and precipitation over the western North Pacific (Fig. 8a), even with opposite correlations in ACCESS1.0 and ACCESS1.3 (Fig. 8a). This implies that only 15 out of 23 models can capture the remarkable precipitation dipole pattern related to the SCSSM.

Previous studies (e.g., Zhang et al. 2018, 2019) indicated that the precipitation dipole served as the primary pathway of the SCSSM affecting JJA IOD. Thus, the relationship between the precipitation dipole and JJA IOD is further examined in Fig. 8b. Like the SCSSM, all correlations between the IOD and precipitation over the Maritime Continent are beyond 95% confidence level during JJA (Fig. 8b). However, only 12 of 23 models studied [i.e., CCSM4, CESM1(FASTCHEM), CNRM-CM5, CSIRO Mk3.6.0, FGOALS-g2, GFDL-ESM2G, HadGEM2-AO, IPSL-CM5A-MR, MPI-ESM-LR, MPI-ESM-MR, MPI-ESM-P, and MRI-CGCM3] successfully simulate the significant correlation between JJA IOD and the western North Pacific precipitation during JJA (Fig. 8b). This suggests that this prominent precipitation dipole is closely associated with JJA IOD in 12 models. Since the SCSSM influences the IOD through the precipitation dipole (e.g., Zhang et al. 2018, 2019), the very different abilities of the individual CMIP5 models to simulate the precipitation dipole pattern imply different influences of the SCSSM on the IOD in individual models.

b. *Physical mechanisms responsible for the effect of the SCSSM on the IOD*

To further demonstrate the aforementioned results, two groups of models were chosen. Although the correlations between the SCSSM and JJA IOD are significant in all models (Fig. 4a), not all significant correlation coefficients may be reasonable. According to our previous studies (e.g., Zhang et al. 2018, 2019), the SCSSM tended to enhance the lower-level wind anomalies over the tropical southeastern Indian Ocean via the precipitation dipole, and then contributed to the development of the IOD events. Furthermore, as removing the precipitation dipole signals, the correlation between the SCSSM and JJA IOD became insignificant (Zhang et al. 2018). This suggests the critical bridge of the precipitation dipole in linking between the SCSSM and JJA IOD. Thus, selecting two types of models takes into consideration not only the relationship between the SCSSM and JJA IOD but also the relevant key physical processes (i.e., the precipitation dipole). Based on the aforementioned analyses, the criterion needs to include the following three conditions: 1) the significant correlation between the SCSSM and JJA IOD, 2) the significant correlations between the SCSSM and precipitation over the western North Pacific and Maritime Continent, and 3) the significant correlations between JJA IOD and precipitation over the western North Pacific and Maritime Continent. This criterion not only highlights the importance of the correlation relationship between the SCSSM and JJA IOD, but also emphasizes the critical underlying physical processes.

Like the significant correlation between the SCSSM and JJA IOD (Fig. 4a), the precipitation over the Maritime Continent is also significantly correlated with both the SCSSMI and JJA DMI in all models (Fig. 8). This suggests that the selection of

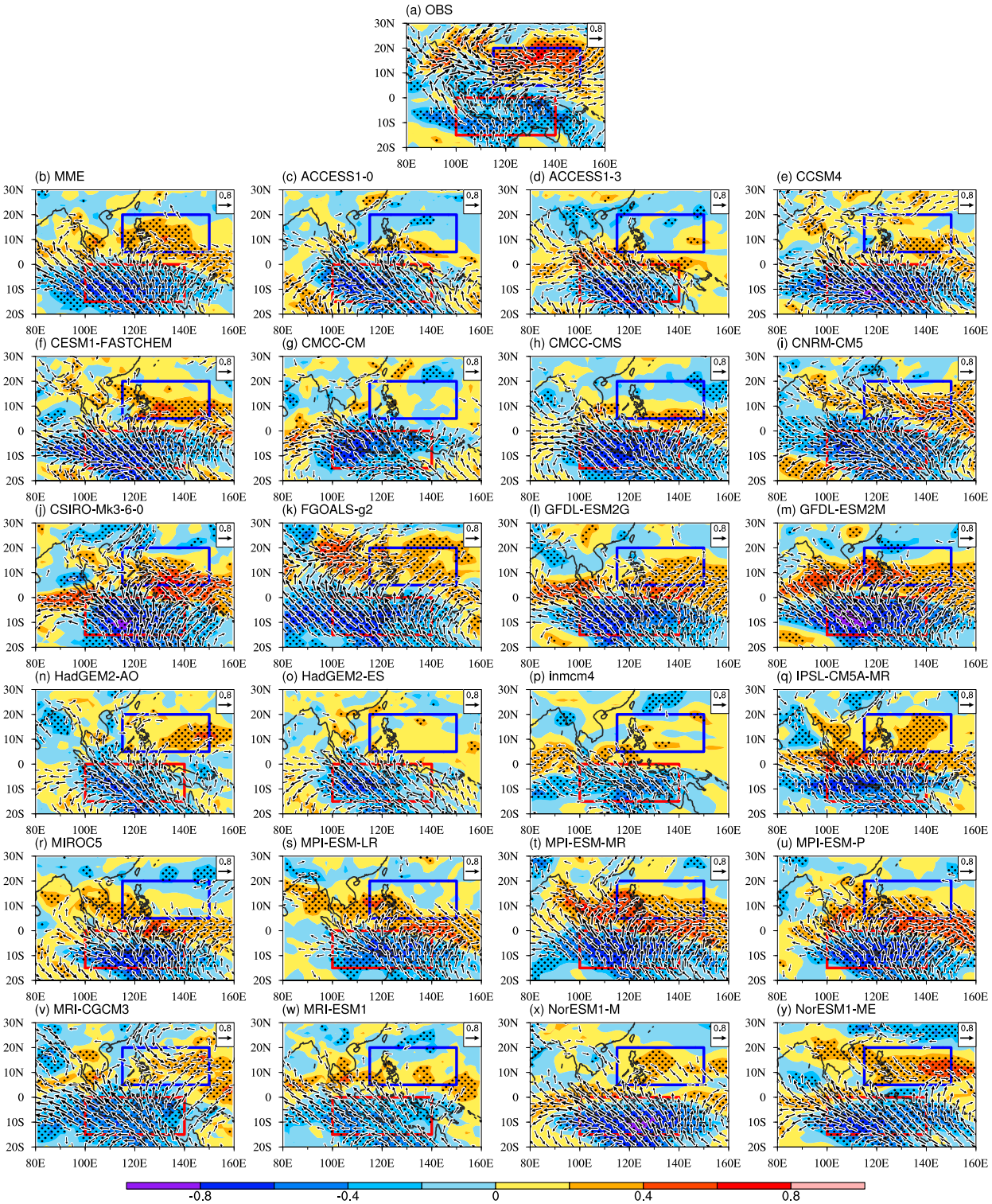

FIG. 6. Correlations of the SCSSMI with the precipitation rate (shading) and 925-hPa wind (vectors) during JJA for (a) the observations (based on NCEP1), (b) the MME mean, and (c)–(y) each CMIP5 model. Black stippling indicates the 95% confidence level, and only wind vectors that are significant at the 95% confidence level are plotted. Red and blue rectangles in (a)–(y) indicate the study areas over the western North Pacific (115°–150°E, 5°–20°N) and Maritime Continent (100°–140°E, 15°S–0°), respectively.

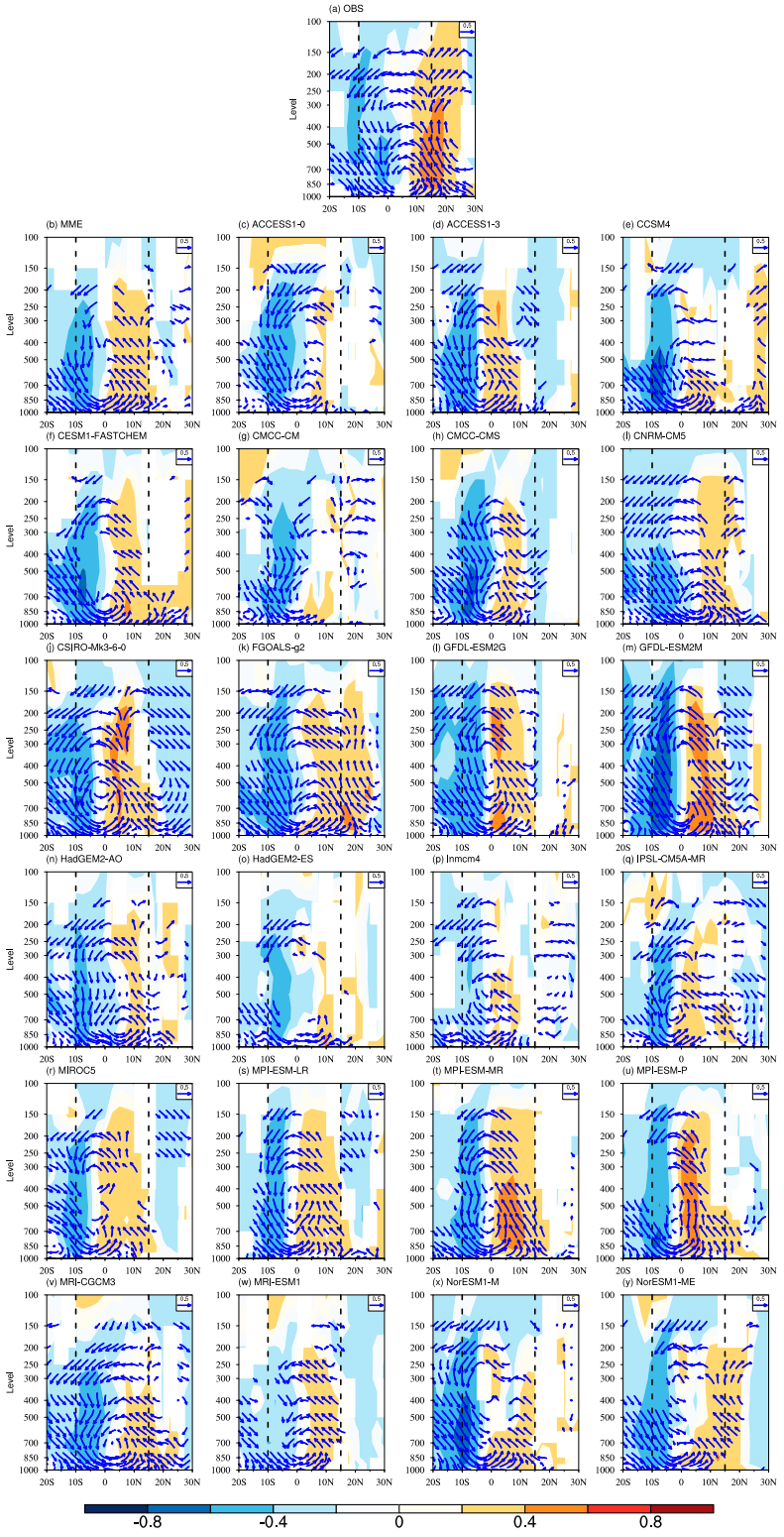

FIG. 7. Correlations of the SCSSMI, as in Fig. 6, with the meridional–vertical circulation anomalies averaged between 100° and 150°E (vectors) and vertical pressure velocity anomalies (shading). Only vertical pressure velocity and wind vectors that are significant at the 95% confidence level are plotted.

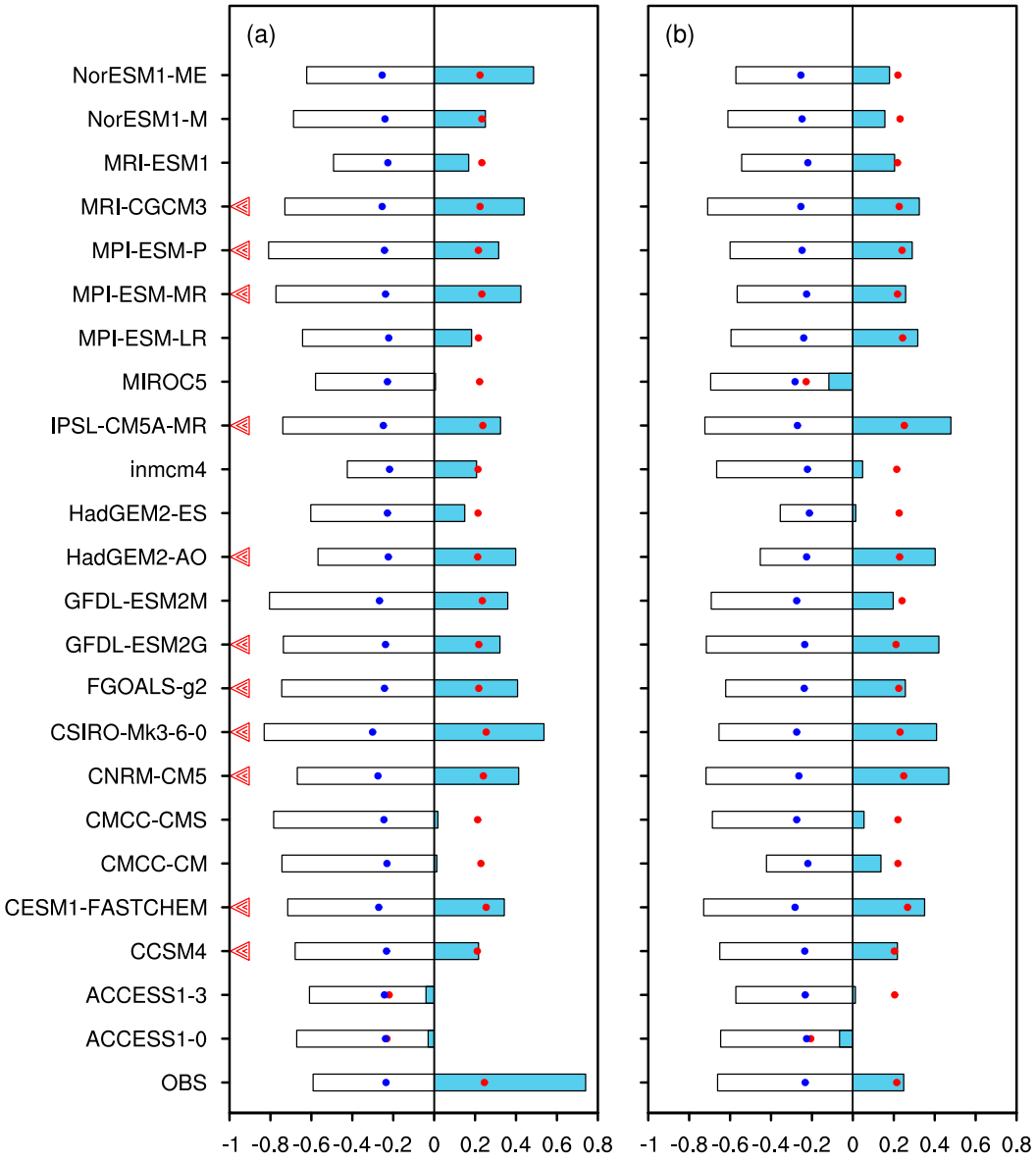

FIG. 8. (a) The correlation coefficients of the SCSSMI with the precipitation area averaged over the western North Pacific (115°–150°E, 5°–20°N; sky blue bars) and Maritime Continent (100°–140°E, 15°S–0°; white bars) during JJA for the observations (OBS) and models. The red (blue) dots in (a) denote the correlations between the SCSSMI and western North Pacific (Maritime Continent) precipitation exceeding the 95% confidence level. (b) As in (a), but for JJA DMI with the precipitation area averaged over the western North Pacific and Maritime Continent. The red triangles in (a) indicate the models that simulate simultaneously the significant correlations between the SCSSM and precipitation over the western North Pacific and Maritime Continent and between JJA IOD and precipitation over the western North Pacific and Maritime Continent.

two types of models is mainly determined by the relationships of the western North Pacific precipitation with the SCSSMI and JJA DMI. Eleven models [i.e., CCSM4, CESM1(FASTCHEM), CNRM-CM5, CSIRO Mk3.6.0, FGOALS-g2, GFDL-ESM2G, HadGEM2-AO, IPSL-CM5A-MR, MPI-ESM-MR, MPI-ESM-P, and MRI-CGCM3] that simulate successfully both the significant correlations of the western North Pacific precipitation with the SCSSMI and JJA DMI are defined as Type I, and the remaining 12 models belong to Type II (i.e., ACCESS1.0, ACCESS1.3, CMCC-CM, CMCC-CMS, HadGEM2-ES, GFDL-ESM2M, INM-CM4.0, MIROC5, MPI-ESM-LR, MRI-ESM1, NorESM1-M, and NorESM1-ME). Meanwhile, the significant reverse correlations in precipitation between the western North Pacific and Maritime Continent exist in all Type I models (not shown), representing reasonably the out-of-phase variation of the precipitation over the western North Pacific

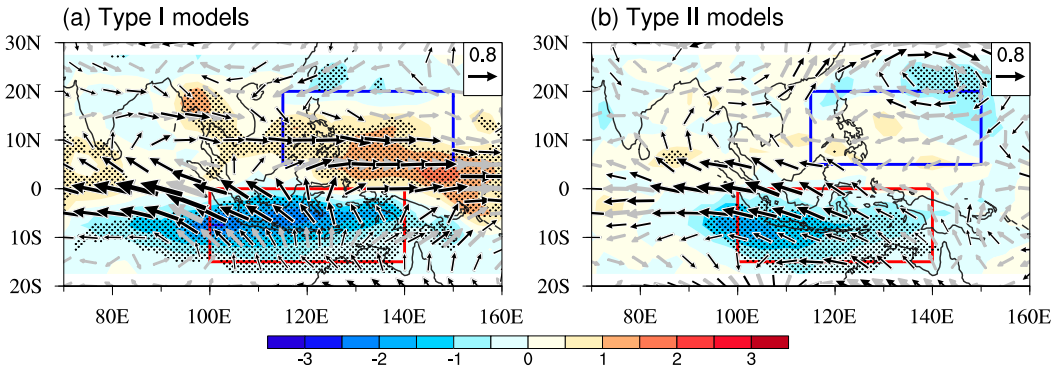

FIG. 9. Regression of the 925-hPa wind (vectors; m s^{-1}) and the precipitation rate (prate; shading; 10^4 kg m^{-2} s^{-1}) onto the SCSSMI for the (a) Type I and (b) Type II models during JJA. Black stippling and bold wind vectors indicate the 95% confidence level. Red and blue rectangles in (a) and (b) indicate the study areas over the western North Pacific (115°–150°E, 5°–20°N) and Maritime Continent (100°–140°E, 15°S–0°), respectively.

and Maritime Continent. It is noted that 8 Type I and 12 Type II models are applied in the following analyses because 3 Type I models [i.e., CCSM4, CESM1(FASTCHEM), and HadGEM2-AO] lack the SSH variable. In addition, these two types of models have the similar amplitude and spatial pattern of the climatological biases in precipitation and 925-hPa winds, and the ratios of the standard deviations between the simulations and observations in climatological precipitation and 925-hPa wind are nearly close to 1.0 in the two types of models (not shown). These indicate the little effects of the climatological biases on the two types of models. The different capabilities of the model ensemble members in simulating the relationships of the precipitation dipole with the SCSSM and IOD can be readily distinguished owing to the selection criteria used; therefore, the disparity of the impact of the SCSSM on the IOD and associated physical mechanisms can be illustrated.

Previous studies have indicated that the enhanced precipitation dipole related to the SCSSM enhances the southeasterly wind anomalies over the tropical southeastern Indian Ocean, further contributing to the growth of the IOD (Zhang et al. 2018, 2019). Figure 9 presents the relationship between the SCSSM and the precipitation over the western North Pacific and Maritime Continent for the two types of models. The precipitation dipole generated by the Type I models is largely consistent with the observations, although there are some biases in its simulated amplitude and location (Fig. 9a). In contrast, the Type II models do not successfully reproduce the precipitation dipole pattern (Fig. 9b). Corresponding to the precipitation dipole, the Type I models simulate a remarkable SCSSM Hadley circulation over the western North Pacific and Maritime Continent, much stronger than that of the Type II models (Fig. 10). Consequently, the southeasterly wind anomalies over the tropical southeastern Indian Ocean in Type I models are much larger than that in Type II models (Fig. 9).

Prior studies have highlighted the significant role of that the anomalous southeasterly wind off the coasts of Sumatra and Java in the development of the IOD (Bjerknes 1969; Huang and Shukla 2007b; Li et al. 2003; Xie et al. 2002; Zhang et al. 2018, 2019); this wind is a major factor in the WES and Bjerknes feedbacks. Southeasterly wind anomalies that are strengthened by the precipitation dipole and the SCSSM Hadley circulation occur over the tropical southeastern Indian Ocean during periods in which the SCSSM is particularly strong (Fig. 6). The increased southeasterly wind anomalies are superimposed on the mean southeasterly wind during JJA and induce increased ocean surface evaporation and a loss of latent ocean heat flux (Fig. 11a). This strengthens localized cold SST anomalies (Fig. 11g). Meanwhile, the enhanced southeasterly wind anomalies also increase local thermocline anomalies (Fig. 11d), and the cold SST anomalies over the tropical southeastern Indian Ocean are strengthened by cold water from the deep ocean (Fig. 11g). The intensity of the IOD events increases in line with the zonal gradient of SST anomalies in the tropical Indian Ocean (Fig. 11g). The aforementioned findings indicate that the SCSSM significantly impacts the IOD development through the positive WES and Bjerknes feedbacks.

Compared with the observations, the southeasterly wind anomalies in the Type I models off the coasts of Sumatra and Java are much stronger, increasing the latent heat flux loss from the ocean (Fig. 11b) and bringing more cold water from the deep ocean to the surface (Fig. 11e). This suggests that the stronger southeasterly wind anomalies lead to larger cold SST anomalies over the tropical southeastern Indian Ocean in the framework of the WES and Bjerknes feedbacks (Fig.11h). Weaker southeasterly wind anomalies, associated with the Type II models (Fig. 11b), produce much weaker WES and Bjerknes feedbacks (Figs. 11c,f), resulting in the smaller cold SST anomalies off Sumatra and Java (Fig. 11i). These qualitative results suggest that the influence of the SCSSM on the JJA IOD in models that can simulate reasonably well the atmospheric bridges related to the SCSSM is much larger than in those that cannot.

We also verify quantitatively the different contributions of the SCSSM to the IOD in the two types of models. Here, the regression coefficients of the precipitation against the SCSSMI area averaged over the western North Pacific and Maritime Continent regions denote the mean intensity of the

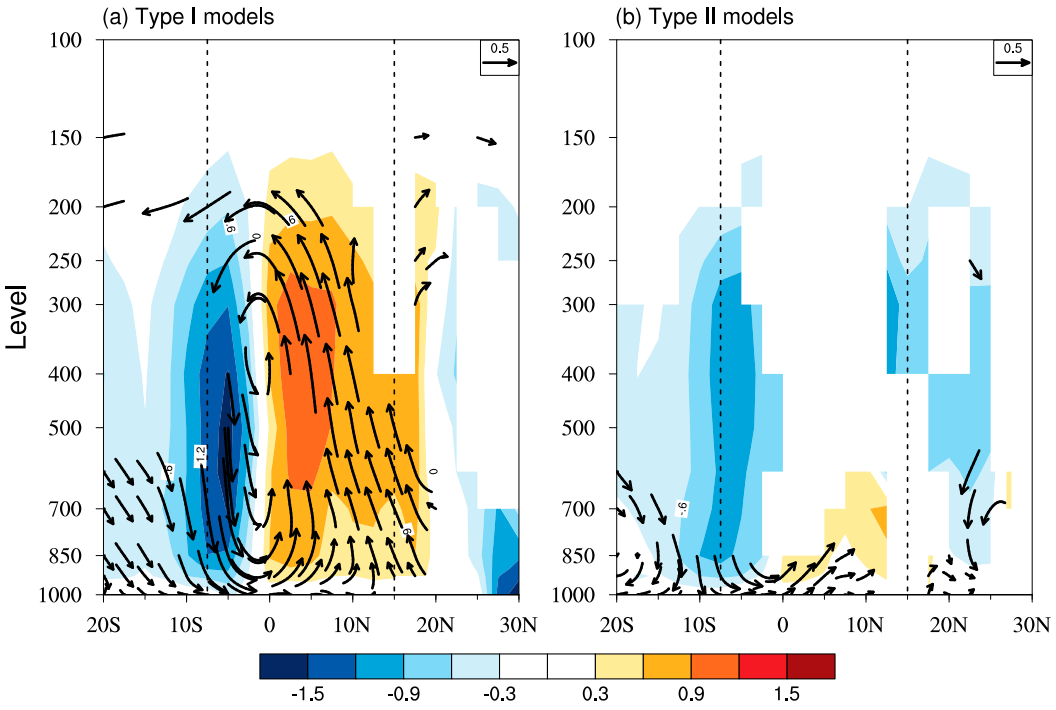

FIG. 10. As in Fig. 9, but for the meridional–vertical circulation anomalies averaged between 100° and 150°E (vectors; m s^{-1}) and vertical pressure velocity anomalies (shading; -10^{-2} Pa s^{-1}). Only vertical pressure velocity and wind vectors that are significant at the 95% confidence level are plotted.

precipitation explained by the SCSSM. Similar calculations may be applied to the 925-hPa zonal and meridional wind anomalies over the tropical southeastern and central Indian Ocean, as summarized in Fig. 12. The observations, Type I, and Type II models can all capture a precipitation dipole pattern, while the western North Pacific precipitation anomalies in Type II models are much weaker than those in observations and Type I models (Fig. 12). This implies that the precipitation gradient over the western North Pacific and Maritime Continent in Type II models is much smaller, leading to weaker southeasterly wind anomalies over the tropical southeastern Indian Ocean (Fig. 12). The maximum precipitation gradient is found in Type I models, corresponding to the largest southeasterly wind anomalies over the tropical southeastern Indian Ocean. The SCSSM contributes less to the equatorial easterly wind anomalies in the central Indian Ocean than to the southeasterly wind anomalies over the tropical southeastern Indian Ocean (Fig. 12). Similar results are also observed for the correlations of the SCSSMI with the precipitation dipole, SCSSM Hadley circulation, and 925-hPa wind over the southeastern Indian Ocean (not shown).

The observed southeasterly wind anomalies favor latent heat loss from the ocean and lift the thermocline anomalies over the tropical southeastern Indian Ocean, further cooling the local cold SST anomalies (Fig. 13a). In Type I models, large latent heat flux and SSH anomalies strengthened by the stronger southeasterly wind anomalies correspond to the significant correlation between the SCSSMI and JJA EDMI, much closer to the observations (Figs. 13a and 14a). On the contrary, the Type II models have small latent heat flux and SSH anomalies due to the weaker southeasterly wind anomalies (Fig. 13a); therefore, the correlation between the SCSSM and JJA EDMI in Type II models are much weaker than in observations and Type I models (Figs. 13a and 14a). Similar results can also be found in SON, although the correlation between the SCSSMI and SON EDMI slightly exceeds 99% confidence level in Type II models (Fig. 14b). This is consistence with the results in Zhang et al. (2018, 2019) where they indicated the SCSSM mainly affecting the east pole of the IOD through the precipitation dipole. The SCSSM has a maximum correlation with the IOD when the former leads the latter 3–4 months (not shown; Zhang et al. 2018), indicating the potential influence of the SCSSM on SON IOD. As the zonal gradient of SST anomalies increases over the tropical Indian Ocean, the western Indian Ocean SST anomalies begin to grow in JJA and mature in SON under the positive WES and Bjerknes feedbacks (Fig. 14b), although the SCSSM has disappeared in SON. As a result, the SCSSMI is significantly correlated with SON WDMI in Type I models, which is comparable to the observation (Fig. 14b). It is noted that the simulated correlation between the SCSSMI and JJA WDMI in the two types of models are both significant and larger than that in observations (Fig. 14a), which may possibly result from the strong warm western Indian Ocean SST bias induced by the weakened southwest summer monsoon (Li et al. 2015, 2016). Overall, when the Type I (Type II) models simulate

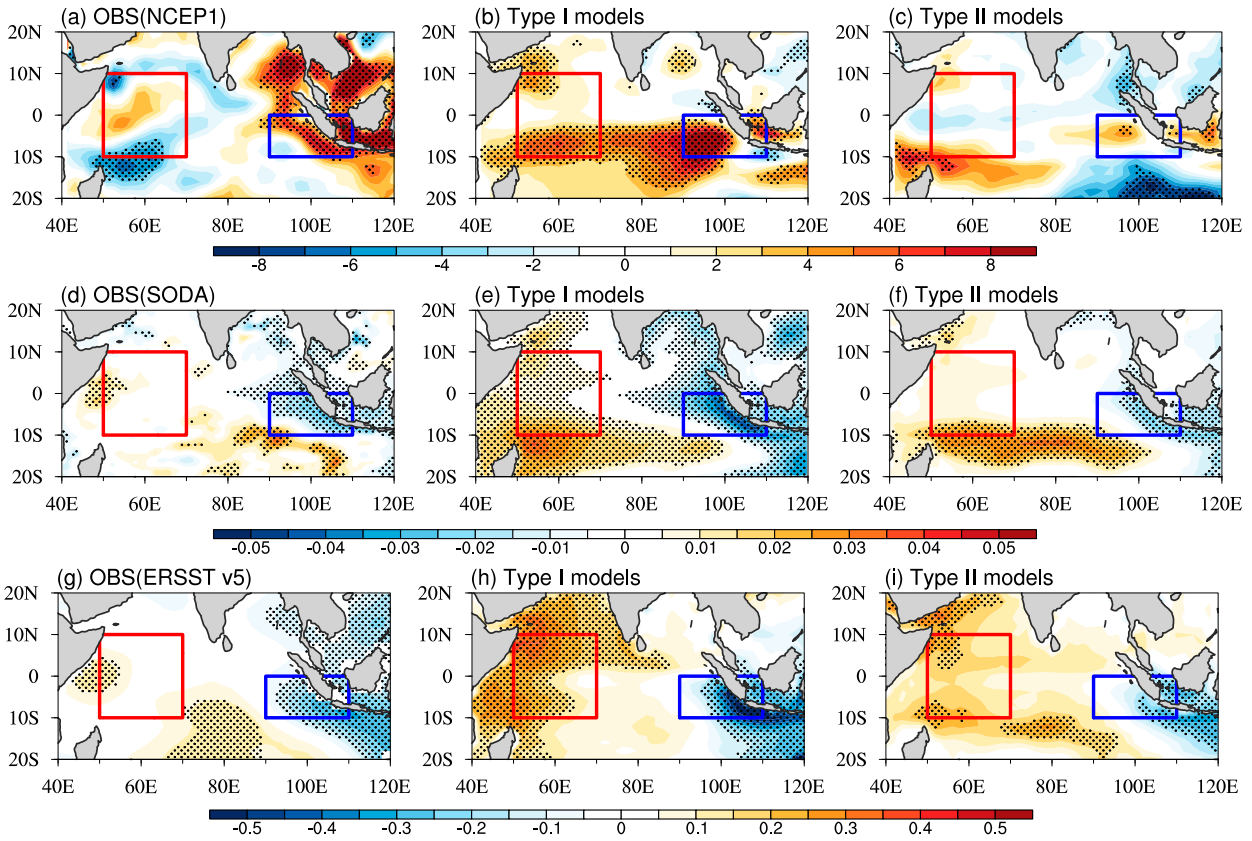

FIG. 11. Regression of the latent heat flux anomalies (shading; W m^{-2}) onto the SCSSMI during JJA for (a) the observations, (b) Type I, and (c) Type II models. (d)–(i) As in (a)–(c), but for the (d)–(f) SSH (m) and (g)–(i) SST (°C) anomalies. Black stippling indicates the 95% confidence level. Red and blue rectangles indicate the study areas over the tropical southeastern (90°–110°E, 10°S–0°) and western (50°–70°E, 10°S–10°N) Indian Ocean, respectively.

successfully (poorly) the precipitation dipole related to the SCSSM and JJA IOD, the SCSSM has the larger (smaller) influence on the IOD, especially for the east pole of the IOD.

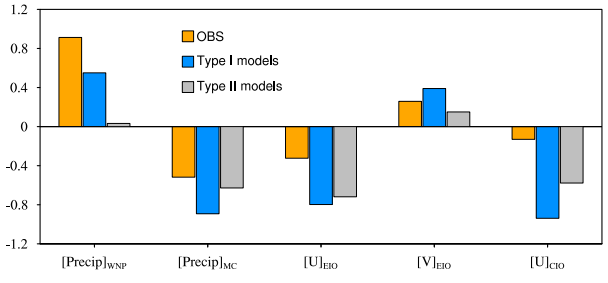

FIG. 12. Area-averaged regression coefficients of the precipitation (Precip; 10^4 kg m^{-2} s^{-1}), 925-hPa zonal wind (U; m s^{-1}), and 925-hPa meridional wind (V; m s^{-1}) anomalies associated with the SCSSM for OBS (orange bars), Type I (blue bars), and Type II (gray bars) models over the key regions indicate their mean intensity during JJA. "WNP" and "MC" indicate the western North Pacific (115°–150°E, 5°–20°N) and Maritime Continent (100°–140°E, 15°S–0°) regions, respectively. similarly, "EIO" and "CIO" denote the tropical southeastern Indian Ocean (90°–110°E, 10°S–0°) and central Indian Ocean (70°–90°E, 5°S–5°N) regions, respectively.

5. Possible effects of the ENSO on the relationship between the SCSSM and IOD

The greatest interannual ocean–atmosphere variability on Earth results from ENSO, which is associated with both the SCSSM (Hu et al. 2014; Klein et al. 1999; Wang et al. 2003, 2009; Xie et al. 2009) and the IOD (Annamalai et al. 2003; Guo et al. 2015; Schott et al. 2009; Stuecker et al. 2017; Wang and Wang 2014; Xie et al. 2002; Yang et al. 2015; Zhang et al. 2015; Zhang et al. 2019). As a result, ENSO's impact on the relationship between the SCSSM and IOD must be considered. Partial correlations of the SCSSM with the JJA and SON IOD are shown in Fig. 15, in which JJA ENSO signals for the period 1948–2005 have been removed. A correlation coefficient of 0.52 can be calculated between the observed SCSSMI and JJA DMI; after the JJA ENSO signal is removed, the correlation coefficient is reduced to 0.49 but remains significant at the 99% confidence level. In the simulations, the correlation between the SCSSM and the JJA IOD remains significant after the JJA ENSO signals are removed in 20 models but becomes insignificant in three of the models (i.e., MIROC5, MPI-ESM-LR, and MPI-ESM-P; Fig. 15a). The SCSSM is still significantly correlated with JJA IOD in at least 19 models even after removal of the preceding winter, spring, following autumn, and winter ENSO signals (Fig. 15a).

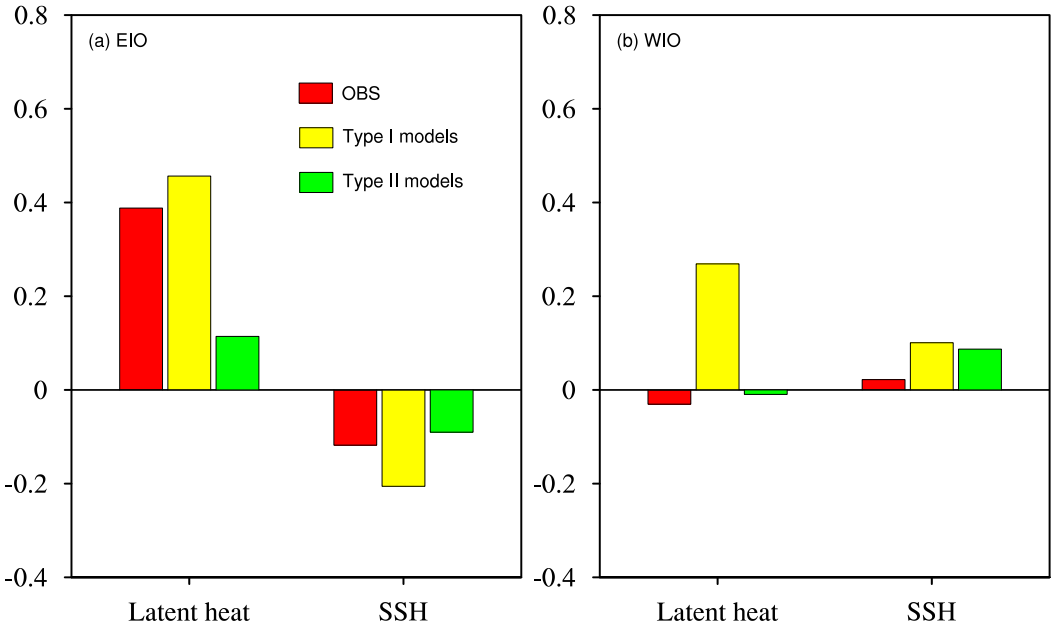

FIG. 13. As in Fig. 12, but for the area-averaged regression coefficients of the latent heat flux (W m^{-2}) and SSH (m) anomalies associated with the SCSSM for OBS (red bars), Type I (yellow bars), and Type II (green bars) models over the tropical (a) southeastern (90°–110°E, 10°S–0°) and (b) western (50°–70°E, 10°S–10°N) Indian Ocean.

In the observations, when the JJA ENSO signals are removed, the SCSSM maintains a coefficient of 0.5, remaining significantly correlated with the SON IOD (Fig. 15b). Four models (INM-CM4.0, MIROC5, MPI-ESM-LR, and MPI-ESM-P) do not show a significant correlation between the SCSSM and the SON IOD; however, 19 models replicate a significant correlation after JJA ENSO signals are removed (Fig. 15b). Furthermore, in at least 19 of the models, the

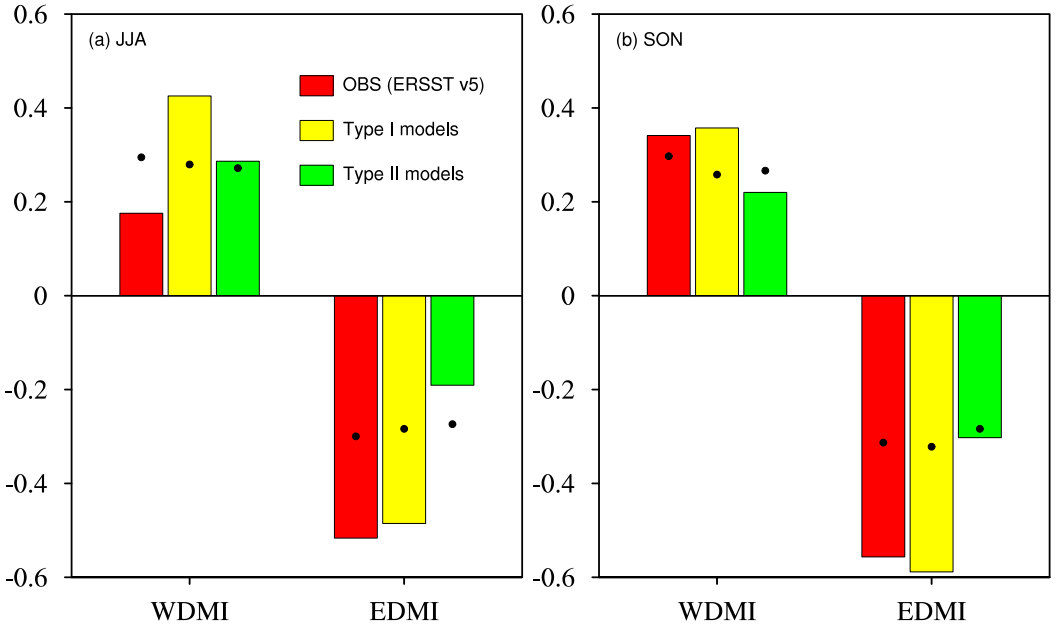

FIG. 14. (a) The correlation coefficients of the SCSSMI with EDMI and WDMI for OBS (red bars), Type I (yellow bars), and Type II (green bars) models during JJA. (b) As in (a), but for SON. Here, the EDMI and WDMI are area averaged over the tropical southeastern (90°–110°E, 10°S–0°) and western (50°–70°E, 10°S–10°N) Indian Ocean, respectively. The black dots in (a) and (b) denote the 99% confidence level.

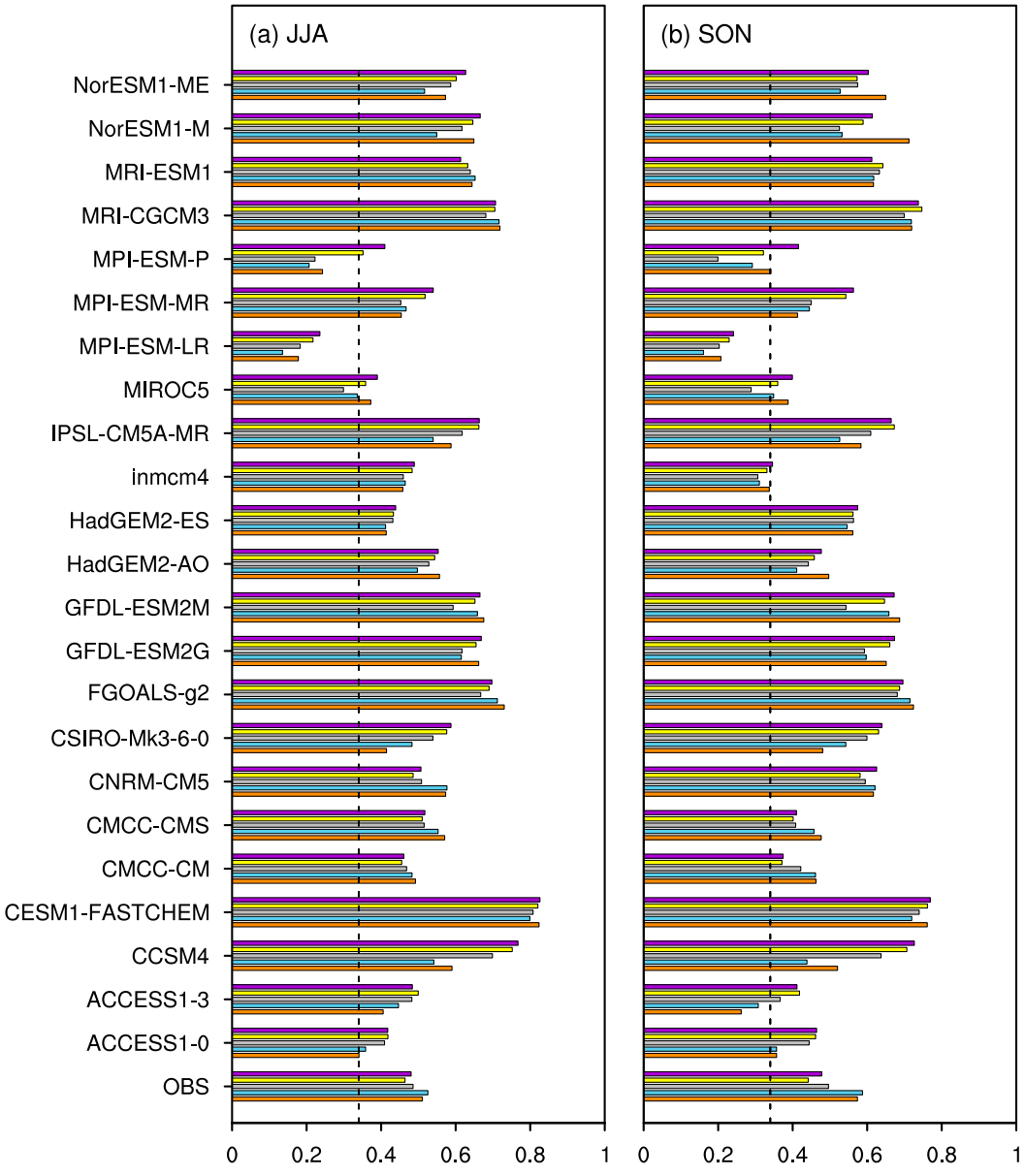

FIG. 15. As in Fig. 4, but for the partial correlation after removing the preceding winter (orange bars), spring (sky blue bars), simultaneous JJA (gray bars), following SON (gray bars), and winter (violet bars) ENSO signals during (a) JJA and (b) SON. Dashed lines indicate the 99% confidence level.

correlation coefficients remain significant between the SCSSMI and SON DMI after the preceding winter and spring and the following autumn and winter ENSO signals are removed (Fig. 15b). Similar results can also be obtained even excluding ENSO signals from both the SCSSM and the IOD by using partial regression analysis (not shown). These results suggest a significant correlation in at least 19 of the models between the SCSSM and the IOD during JJA and SON, despite the slight weakening effect of the ENSO on the relationship between the IOD and the SCSSM.

6. Summary and discussion

Recent studies using observational datasets have reported that the precipitation dipole and SCSSM Hadley circulation play essential roles in the influence of the SCSSM on the IOD (Zhang et al. 2018, 2019). Whether this observed relationship between the SCSSM and the IOD can be successfully reproduced in CMIP5 models is unclear. This study systematically evaluates the impact of the SCSSM on the IOD and the relevant physical mechanisms using 23 CMIP5 models.

First, we assess the climatology of the JJA 925-hPa wind and precipitation and the IOD spatial patterns simulated by the CMIP5 models. The spatial patterns of the JJA 925-hPa wind and precipitation over the SCSSM-related domain (90°–160°E, 20°S–30°N) are basically consistent with the observed data, especially for the zonal wind with a spatial correlation coefficient exceeding 0.85. Moreover, the models can capture reasonably the maximum precipitation centers of the western North Pacific Ocean, South China Sea, and northeastern Bay of Bengal. For the IOD, the zonal seesaw structure over the tropical Indian Ocean is reasonably well reproduced. In the observations, the models tend to portray the essential large-scale climate features accurately, notwithstanding some magnitude biases. The capabilities of the CMIP5 models in examining the relationship between the SCSSM and the IOD can therefore be reliably assessed on this basis.

The significant correlations of the SCSSM with the JJA and SON IOD can be reproduced in all models. However, not all the significant correlations may be reasonable in models. Our previous studies (e.g., Zhang et al. 2018, 2019) indicated that the SCSSM favors the lower-level wind anomalies over the tropical southeastern Indian Ocean through the precipitation dipole, and then enhances the development of the IOD events. Furthermore, after removing the precipitation dipole signals, the significant correlation between the SCSSM and JJA IOD disappears (Zhang et al. 2018). This suggests that the precipitation dipole acts as the bridge linking between the SCSSM and JJA IOD. Of the 23 models, 15 models [i.e., CCSM4, CESM1(FASTCHEM), CNRM-CM5, CSIRO Mk3.6.0, FGOALS-g2, GFDL-ESM2G, GFDL-ESM2M, HadGEM2-AO, INM-CM4.0, IPSL-CM5A-MR, MPI-ESM-MR, MPI-ESM-P, MRI-CGCM3, NorESM1-M, and NorESM1-ME) can successfully simulate the precipitation dipole pattern related to the SCSSM. Similarly, the significant correlations of the IOD with precipitation over the western North Pacific and Maritime Continent during JJA in 12 out of 23 models [i.e., CCSM4, CESM1(FASTCHEM), CNRM-CM5, CSIRO Mk3.6.0, FGOALS-g2, GFDL-ESM2G, HadGEM2-AO, IPSL-CM5A-MR, MPI-ESM-LR, MPI-ESM-MR, MPI-ESM-P, and MRI-CGCM3]. In brief, the contrasting abilities in simulating the precipitation dipole pattern in each CMIP5 model suggest the distinct influence of the SCSSM on the IOD.

To further explore the different influence of the SCSSM on the IOD in CMIP5 models, two categories of models are defined according to their performance in simulating the correlations between the SCSSM and JJA IOD, between the SCSSM and the precipitation over the western North Pacific and Maritime Continent, and between JJA IOD and the precipitation over the western North Pacific and Maritime Continent. In line with the observations, dipole patterns of precipitation anomalies in the Type I models are evident and correspond to the significant SCSSM Hadley circulation during JJA. The southeasterly wind anomalies intensified by the precipitation dipole and SCSSM Hadley circulation off Sumatra and Java coasts tend to enhance the local cold SST anomalies via positive WES and Bjerknes feedbacks. Compared with the Type I models, the southeasterly wind anomalies over the tropical southeastern Indian Ocean in Type II models are weaker because of the poor simulation of the precipitation dipole pattern. The corresponding WES and Bjerknes feedbacks are much weaker, causing the relatively smaller cold SST anomalies over the tropical southeastern Indian Ocean. In SON, the Type I models still have the maximum intensity based on the positive Bjerknes feedback. In summary, the better the models simulate the precipitation dipole pattern associated with the SCSSM and JJA IOD, the larger the SCSSM impacts on the IOD, especially for the east pole of the IOD.

The Type I models have been proved to be relatively accurate, although some discrepancies cannot be ignored. For instance, compared with the observations, the precipitation anomalies over the western North Pacific (Maritime Continent) are evidently underestimated (overestimated). Moreover, there is an obvious equatorward shift of the precipitation anomalies over the SCSSM-related region (90°–160°E, 20°S–30°N), especially over the western North Pacific where the southerly biases are larger. This southward shift of the precipitation may be related to incorrect simulation of the western Pacific anticyclone in CMIP5 (Song and Zhou 2014a,b), which could be traced back to the excessive mean error of the equatorial Pacific cold tongue (Li et al. 2019). Whether the Pacific cold tongue biases affect the relationship between the SCSSM and the IOD needs to be investigated further.

The potential influences of the ENSO on the relationship between the SCSSM and IOD are also examined in this study. At least 19 out of 23 models can reproduce the significant correlation between the SCSSM and IOD during JJA and SON after removing ENSO signals from the preceding winter to following winter. This indicates the relationship between the SCSSM and IOD is little affected by the ENSO signals. Recently, Zhang et al. (2019) indicated that the SCSSM and ENSO have individual and synergistic effects on IOD development. Moreover, the improved models being run in the CMIP6 project set up by the WCRP are providing additional data to help explore this issue in the future (Simpkins 2017; Zhou et al. 2019). The individual and synergistic effects of the SCSSM and ENSO on IOD development in CMIP5 and CMIP6 models require further systematic study.

Acknowledgments. This work was jointly sponsored by the National Natural Science Foundation of China (NSFC) Project (41530424, 41790474), Shandong Natural Science Foundation Project (ZR2019ZD12), and Fundamental Research Funds for the Central Universities (201962009, 842113001). We are grateful for the atmospheric variables including wind, precipitation rate, and net surface latent heat flux from NCEP–NCAR, precipitation from CMAP, SST from NOAA and the Met Office Hadley Centre, and SSH from SODA. We also acknowledge the WCRP's Working Group on Coupled Modelling, which is responsible for CMIP, and the climate modeling groups listed in Table 1 for making the WCRP model output available (https://esgf-node.llnl.gov/search/cmip5/).

REFERENCES

Annamalai, H., R. Murtugudde, J. Potemra, S. P. Xie, P. Liu, and B. Wang, 2003: Coupled dynamics over the Indian Ocean: Spring initiation of the zonal mode. *Deep-Sea Res. II*, **50**, 2305–2330, https://doi.org/10.1016/S0967-0645(03)00058-4.

Ashok, K., Z. Y. Guan, and T. Yamagata, 2003: Influence of the Indian Ocean dipole on the Australian winter rainfall. *Geophys. Res. Lett.*, **30**, 1821, https://doi.org/10.1029/2003GL017926.

——, ——, N. H. Saji, and T. Yamagata, 2004: Individual and combined influences of ENSO and the Indian Ocean dipole on the Indian summer monsoon. *J. Climate*, **17**, 3141–3155, https://doi.org/10.1175/1520-0442(2004)017<3141:IACIOE>2.0.CO;2.

Behera, S. K., J. J. Luo, S. Masson, S. A. Rao, H. Sakuma, and T. Yamagata, 2006: A CGCM study on the interaction between IOD and ENSO. *J. Climate*, **19**, 1688–1705, https://doi.org/10.1175/JCLI3797.1.

Bjerknes, J., 1969: Atmospheric teleconnections from the equatorial Pacific. *Mon. Wea. Rev.*, **97**, 163–172, https://doi.org/10.1175/1520-0493(1969)097<0163:ATFTEP>2.3.CO;2.

Bretherton, C. S., M. Widmann, V. P. Dymnidov, J. M. Wallace, and I. Bladé, 1999: The effective number of spatial degrees of freedom of a time-varying field. *J. Climate*, **12**, 1990–2009, https://doi.org/10.1175/1520-0442(1999)012<1990:TENOSD>2.0.CO;2.

Cai, W. J., T. Cowan, and A. Sullivan, 2009: Recent unprecedented skewness towards positive Indian Ocean dipole occurrences and its impact on Australian rainfall. *Geophys. Res. Lett.*, **36**, L11705, https://doi.org/10.1029/2009GL037604.

——, P. van Rensch, T. Cowan, and H. Hendon, 2011: Teleconnection pathways of ENSO and the IOD and the mechanisms for impacts on Australian rainfall. *J. Climate*, **24**, 3910–3923, https://doi.org/10.1175/2011JCLI4129.1.

——, X. T. Zheng, E. Weller, M. Collins, T. Cowan, M. Lengaigne, W. D. Yu, and T. Yamagata, 2013: Projected response of the Indian Ocean dipole to greenhouse warming. *Nat. Geosci.*, **6**, 999–1007, https://doi.org/10.1038/ngeo2009.

——, A. Santoso, G. Wang, E. Weller, L. Wu, K. Ashok, Y. Masumoto, and T. Yamagata, 2014: Increased frequency of extreme Indian Ocean dipole events due to greenhouse warming. *Nature*, **510**, 254–258, https://doi.org/10.1038/nature13327.

——, and Coauthors, 2018: Stabilised frequency of extreme positive Indian Ocean dipole under 1.5°C warming. *Nat. Commun.*, **9**, 1419, https://doi.org/10.1038/s41467-018-03789-6.

Carton, J. A., and B. S. Giese, 2008: A reanalysis of ocean climate using Simple Ocean Data Assimilation (SODA). *Mon. Wea. Rev.*, **136**, 2999–3017, https://doi.org/10.1175/2007MWR1978.1.

Chen, J. P., J. Y. Yu, X. Wang, and T. Lian, 2020: Different influences of southeastern Indian Ocean and western Indian Ocean SST anomalies on eastern China rainfall during the decaying summer of 2015/16 extreme El Niño. *J. Climate*, **33**, 5427–5443, https://doi.org/10.1175/JCLI-D-19-0777.1.

Ding, R. Q., K. J. Ha, and J. P. Li, 2010: Interdecadal shift in the relationship between the East Asian summer monsoon and the tropical Indian Ocean. *Climate Dyn.*, **34**, 1059–1071, https://doi.org/10.1007/s00382-009-0555-2.

Duan, J., Y. L. Li, L. Zhang, and F. Wang, 2020: Impacts of the Indian Ocean dipole on sea level and gyre circulation of the western tropical Pacific Ocean. *J. Climate*, **33**, 4207–4228, https://doi.org/10.1175/JCLI-D-19-0782.1.

Fan, L., Q. Liu, C. Wang, and F. Guo, 2017: Indian Ocean dipole modes associated with different types of ENSO development. *J. Climate*, **30**, 2233–2249, https://doi.org/10.1175/JCLI-D-16-0426.1.

Guan, Z. Y., and T. Yamagata, 2003: The unusual summer of 1994 in East Asia: IOD teleconnections. *Geophys. Res. Lett.*, **30**, 1544, https://doi.org/10.1029/2002GL016831.

Guo, F. Y., Q. Liu, S. Sun, and J. Yang, 2015: Three types of Indian Ocean dipoles. *J. Climate*, **28**, 3073–3092, https://doi.org/10.1175/JCLI-D-14-00507.1.

Hu, K., G. Huang, X.-T. Zheng, S.-P. Xie, X. Qu, Y. Du, and L. Liu, 2014: Interdecadal variations in ENSO influences on northwest Pacific–East Asian early summertime climate simulated in CMIP5 models. *J. Climate*, **27**, 5982–5998, https://doi.org/10.1175/JCLI-D-13-00268.1.

——, ——, S.-P. Xie, and S.-M. Long, 2019: Effect of the mean flow on the anomalous anticyclone over the Indo-northwest Pacific in post-El Niño summers. *Climate Dyn.*, **53**, 5725–5741, https://doi.org/10.1007/s00382-019-04893-z.

Huang, B. H., and J. Shukla, 2007a: Mechanisms for the interannual variability in the tropical Indian Ocean. Part I: The role of remote forcing from the tropical Pacific. *J. Climate*, **20**, 2917–2936, https://doi.org/10.1175/JCLI4151.1.

——, and ——, 2007b: Mechanisms for the interannual variability in the tropical Indian Ocean. Part II: Regional processes. *J. Climate*, **20**, 2937–2960, https://doi.org/10.1175/JCLI4169.1.

Huang, B. Y., P. W. Thorne, V. F. Banzon, T. Boyer, and H. M. Zhang, 2017: Extended Reconstructed Sea Surface Temperature, version 5 (ERSST v5): Upgrades, validations, and intercomparisons. *J. Climate*, **30**, 8179–8205, https://doi.org/10.1175/JCLI-D-16-0836.1.

Kalnay, E., and Coauthors, 1996: The NCEP/NCAR 40-Year Reanalysis Project. *Bull. Amer. Meteor. Soc.*, **77**, 437–471, https://doi.org/10.1175/1520-0477(1996)077<0437:TNYRP>2.0.CO;2.

Kanamitsu, M., W. Ebisuzaki, J. Woollen, S. Yang, J. Hnilo, M. Fiorino, and G. Potter, 2002: NCEP–DOE AMIP-II Reanalysis (R-2). *Bull. Amer. Meteor. Soc.*, **83**, 1631–1644, https://doi.org/10.1175/BAMS-83-11-1631.

Klein, S. A., B. J. Soden, and N.-C. Lau, 1999: Remote sea surface temperature variations during ENSO: Evidence for a tropical atmospheric bridge. *J. Climate*, **12**, 917–932, https://doi.org/10.1175/1520-0442(1999)012<0917:RSSTVD>2.0.CO;2.

Krishnamurthy, V., and B. P. Kirtman, 2003: Variability of the Indian Ocean: Relation to monsoon and ENSO. *Quart. J. Roy. Meteor. Soc.*, **129**, 1623–1646, https://doi.org/10.1256/qj.01.166.

Li, G., S.-P. Xie, and Y. Du, 2015: Monsoon-induced biases of climate models over the tropical Indian Ocean. *J. Climate*, **28**, 3058–3072, https://doi.org/10.1175/JCLI-D-14-00740.1.

——, ——, and ——, 2016: A robust but spurious pattern of climate change in model projections over the tropical Indian Ocean. *J. Climate*, **29**, 5589–5608, https://doi.org/10.1175/JCLI-D-15-0565.1.

——, ——, C. He, and Z. Chen, 2017: Western Pacific emergent constraint lowers projected increase in Indian summer monsoon rainfall. *Nat. Climate Change*, **7**, 708–712, https://doi.org/10.1038/nclimate3387.

——, and Coauthors, 2019: Effect of excessive equatorial Pacific cold tongue bias on the El Niño-northwest Pacific summer monsoon relationship in CMIP5 multi-model ensemble. *Climate Dyn.*, **52**, 6195–6212, https://doi.org/10.1007/s00382-018-4504-9.

Li, J. P., and Q. C. Zeng, 2002: A unified monsoon index. *Geophys. Res. Lett.*, **29**, 1274, https://doi.org/10.1029/2001GL013874.

——, and ——, 2003: A new monsoon index and the geographical distribution of the global monsoons. *Adv. Atmos. Sci.*, **20**, 299–302, https://doi.org/10.1007/s00376-003-0016-5.

——, G. X. Wu, and D. X. Hu, 2011a: *Ocean-Atmosphere Interaction over the Joining Area of Asia and Indian-Pacific Ocean and Its Impact on the Short-Term Climate Variation in China* (in Chinese). Vol. 1, China Meteorological Press, 516 pp.

——, ——, and ——, 2011b: *Ocean-Atmosphere Interaction over the Joining Area of Asia and Indian-Pacific Ocean and Its Impact on the Short-Term Climate Variation in China* (in Chinese). Vol. 2, China Meteorological Press, 565 pp.

——, C. Sun, and F. F. Jin, 2013: NAO implicated as a predictor of Northern Hemisphere mean temperature multi-decadal variability. *Geophys. Res. Lett.*, **40**, 5497–5502, https://doi.org/10.1002/2013GL057877.

Li, T., B. Wang, C.-P. Chang, and Y. Zhang, 2003: A theory for the Indian Ocean dipole–zonal mode. *J. Atmos. Sci.*, **60**, 2119–2135, https://doi.org/10.1175/1520-0469(2003)060<2119:ATFTIO>2.0.CO;2.

Liu, L., W. Yu, and T. Li, 2011: Dynamic and thermodynamic air–sea coupling associated with the Indian Ocean dipole diagnosed from 23 WCRP CMIP3 models. *J. Climate*, **24**, 4941–4958, https://doi.org/10.1175/2011JCLI4041.1.

——, S. P. Xie, X. T. Zheng, T. Li, Y. Du, G. Huang, and W. Yu, 2014: Indian Ocean variability in the CMIP5 multi-model ensemble: The zonal dipole mode. *Climate Dyn.*, **43**, 1715–1730, https://doi.org/10.1007/s00382-013-2000-9.

Nuncio, M., and X. Yuan, 2015: The influence of the Indian Ocean dipole on Antarctic sea ice. *J. Climate*, **28**, 2682–2690, https://doi.org/10.1175/JCLI-D-14-00390.1.

Rayner, N. A., D. E. Parker, E. B. Horton, C. K. Folland, L. V. Alexander, D. P. Rowell, E. C. Kent, and A. Kaplan, 2003: Global analyses of sea surface temperature, sea ice, and night marine air temperature since the late nineteenth century. *J. Geophys. Res.*, **108**, 4407, https://doi.org/10.1029/2002JD002670.

Saji, N. H., and T. Yamagata, 2003: Structure of SST and surface wind variability during Indian Ocean dipole mode events: COADS observations. *J. Climate*, **16**, 2735–2751, https://doi.org/10.1175/1520-0442(2003)016<2735:SOSASW>2.0.CO;2.

——, B. N. Goswami, P. N. Vinayachandran, and T. Yamagata, 1999: A dipole mode in the tropical Indian Ocean. *Nature*, **401**, 360–363, https://doi.org/10.1038/43854.

Schott, F. A., S. P. Xie, and J. P. McCreary Jr., 2009: Indian Ocean circulation and climate variability. *Rev. Geophys.*, **47**, RG1002, https://doi.org/10.1029/2007RG000245.

Simpkins, G., 2017: Progress in climate modeling. *Nat. Climate Change*, **7**, 684–685, https://doi.org/10.1038/nclimate3398.

Song, F. F., and T. J. Zhou, 2014a: Interannual variability of East Asian summer monsoon simulated by CMIP3 and CMIP5 AGCMs: Skill dependence on Indian Ocean–western Pacific anticyclone teleconnection. *J. Climate*, **27**, 1679–1697, https://doi.org/10.1175/JCLI-D-13-00248.1.

——, and ——, 2014b: The climatology and interannual variability of East Asian summer monsoon in CMIP5 coupled models: Does air–sea coupling improve the simulations? *J. Climate*, **27**, 8761–8777, https://doi.org/10.1175/JCLI-D-14-00396.1.

Stuecker, M. F., A. Timmermann, F.-F. Jin, Y. Chikamoto, W. Zhang, A. T. Wittenberg, E. Widiasih, and S. Zhao, 2017: Revisiting ENSO/Indian Ocean dipole phase relationships. *Geophys. Res. Lett.*, **44**, 2481–2492, https://doi.org/10.1002/2016GL072308.

Taylor, K. E., 2001: Summarizing multiple aspects of model performance in a single diagram. *J. Geophys. Res.*, **106**, 7183–7192, https://doi.org/10.1029/2000JD900719.

——, R. J. Stouffer, and G. A. Meehl, 2012: An overview of CMIP5 and the experiment design. *Bull. Amer. Meteor. Soc.*, **93**, 485–498, https://doi.org/10.1175/BAMS-D-11-00094.1.

Wang, B., R. G. Wu, and K. M. Lau, 2001: Interannual variability of the Asian summer monsoon: Contrasts between the Indian and the western North Pacific–East Asian monsoons. *J. Climate*, **14**, 4073–4090, https://doi.org/10.1175/1520-0442(2001)014<4073:IVOTAS>2.0.CO;2.

——, ——, and T. Li, 2003: Atmosphere–warm ocean interaction and its impacts on Asian–Australian monsoon variation. *J. Climate*, **16**, 1195–1211, https://doi.org/10.1175/1520-0442(2003)16<1195:AOIAII>2.0.CO;2.

——, F. Huang, Z. Wu, J. Yang, X. Fu, and K. Kikuchi, 2009: Multi-scale climate variability of the South China Sea monsoon: A review. *Dyn. Atmos. Oceans*, **47**, 15–37, https://doi.org/10.1016/j.dynatmoce.2008.09.004.

Wang, X., and C. Wang, 2014: Different impacts of various El Niño events on the Indian Ocean dipole. *Climate Dyn.*, **42**, 991–1005, https://doi.org/10.1007/s00382-013-1711-2.

Webster, P. J., A. M. Moore, J. P. Loschnigg, and R. R. Leben, 1999: Coupled ocean–atmosphere dynamics in the Indian Ocean during 1997–98. *Nature*, **401**, 356–360, https://doi.org/10.1038/43848.

Xie, P., and P. A. Arkin, 1997: Global precipitation: A 17-year monthly analysis based on gauge observations, satellite estimates, and numerical model outputs. *Bull. Amer. Meteor. Soc.*, **78**, 2539–2558, https://doi.org/10.1175/1520-0477(1997)078<2539:GPAYMA>2.0.CO;2.

Xie, S.-P., H. Annamalai, F. A. Schott, and J. P. McCreary Jr., 2002: Structure and mechanisms of south Indian Ocean climate variability. *J. Climate*, **15**, 864–878, https://doi.org/10.1175/1520-0442(2002)015<0864:SAMOSI>2.0.CO;2.

——, K. M. Hu, J. Hafner, H. Tokinaga, Y. Du, G. Huang, and T. Sampe, 2009: Indian Ocean capacitor effect on Indo-western Pacific climate during the summer following El Niño. *J. Climate*, **22**, 730–747, https://doi.org/10.1175/2008JCLI2544.1.

Yamagata, T., S. K. Behera, S. A. Rao, Z. Y. Guan, K. Ashok, and H. N. Saji, 2003: Comments on "Dipoles, temperature gradients, and tropical climate anomalies." *Bull. Amer. Meteor. Soc.*, **84**, 1418–1422, https://doi.org/10.1175/BAMS-84-10-1418.

Yang, Y., S. P. Xie, L. Wu, Y. Kosaka, N.-C. Lau, and G. A. Vecchi, 2015: Seasonality and predictability of the Indian Ocean dipole mode: ENSO forcing and internal variability. *J. Climate*, **28**, 8021–8036, https://doi.org/10.1175/JCLI-D-15-0078.1.

Yu, L., 2003: Variability of the depth of the 20°C isotherm along 68°N in the Bay of Bengal: Its response to remote and local forcing and its relation to satellite SSH variability. *Deep-Sea Res. II*, **50**, 2285–2304, https://doi.org/10.1016/S0967-0645(03)00057-2.

Zhang, W. J., Y. Wang, F. F. Jin, M. F. Stuecker, and A. G. Turner, 2015: Impact of different El Niño types on the El Niño/IOD relationship. *Geophys. Res. Lett.*, **42**, 8570–8576, https://doi.org/10.1002/2015GL065703.

Zhang, Y. Z., J. P. Li, J. Q. Xue, J. Feng, Q. Y. Wang, Y. D. Xu, and Y. H. Wang, 2018: Impact of the South China Sea summer monsoon on the Indian Ocean dipole. *J. Climate*, **31**, 6557–6573, https://doi.org/10.1175/JCLI-D-17-0815.1.

——, ——, ——, F. Zheng, R. G. Wu, K. J. Ha, and J. Feng, 2019: The relative roles of the South China Sea summer monsoon and ENSO in the Indian Ocean dipole development. *Climate Dyn.*, **53**, 6665–6680, https://doi.org/10.1007/s00382-019-04953-4.

Zhou, T. J., L. W. Zou, and X. L. Chen, 2019: Commentary on the Coupled Model Intercomparison Project Phase 6 (CMIP6) (in Chinese). *Climate Change Res.*, **15**, 445–456, https://doi.org/10.12006/j.issn.1673-1719.2019.193.